



1 **Do surface lateral flows matter for data assimilation of soil moisture observations**

2 **into hyperresolution land models?**

3 **Running title: HYPERRESOLUTION LAND DATA ASSIMILATION**

4 Yohei Sawada^{1,2},

5 ¹ Institute of Engineering Innovation, the University of Tokyo, Tokyo, Japan

6 ² Meteorological Research Institute, Japan Meteorological Agency, Tsukuba, Japan

7

8

9 Corresponding author: Y. Sawada, Institute of Engineering Innovation, the University of

10 Tokyo, Tokyo, Japan, 2-11-6, Yayoi, Bunkyo-ku, Tokyo, Japan, yohei.sawada@sogo.t.u-tokyo.ac.jp

11 [tokyo.ac.jp](http://sogo.t.u-tokyo.ac.jp)

12



13 **Abstract**

14 It is expected that hyperresolution land modeling substantially innovates the simulation
15 of terrestrial water, energy, and carbon cycles. The major advantage of hyperresolution
16 land models against conventional one-dimensional land surface models is that
17 hyperresolution land models can explicitly simulate lateral water flows. Despite many
18 efforts on data assimilation of hydrological observations into those hyperresolution land
19 models, how surface water flows driven by local topography matter for data assimilation
20 of soil moisture observations has not been fully clarified. Here I perform two minimalist
21 synthetic experiments where soil moisture observations are assimilated into an integrated
22 surface-groundwater land model by an ensemble Kalman filter. I discuss how differently
23 the ensemble Kalman filter works when surface lateral flows are switched on and off. A
24 horizontal background error covariance provided by overland flows is important to adjust
25 the unobserved state variables (pressure head and soil moisture) and parameters (saturated
26 hydraulic conductivity). However, the non-Gaussianity of the background error provided
27 by the nonlinearity of a topography-driven surface flow harms the performance of data
28 assimilation. It is difficult to efficiently constrain model states at the edge of the area
29 where the topography-driven surface flow reaches by linear-Gaussian filters. It brings the



30 new challenge in land data assimilation for hyperresolution land models. This study

31 highlights the importance of surface lateral flows in hydrological data assimilation.

32

33

34 **1. Introduction**

35 Hyperresolution land modeling is expected to improve the simulation of terrestrial water,

36 energy, and carbon cycles, which is crucially important for meteorological, hydrological

37 and ecological applications (see Wood et al. (2011) for a comprehensive review). While

38 conventional land surface models (LSMs) assume that lateral water flows are negligible

39 at the coarse resolution (>25km) and solve vertical one-dimensional Richards equation

40 for the soil moisture simulation (e.g., Sellers et al. 1996; Lawrence et al. 2011), currently

41 proposed hyperresolution land models, which can be applied at a finer resolution (<1km),

42 explicitly consider surface and subsurface lateral water flows (e.g., Maxwell and Miller

43 2005; Tian et al. 2012; Shrestha et al. 2014; Niu et al. 2014). The fine horizontal resolution

44 can resolve slopes, which are drivers of a lateral transport of water, and realize the fully

45 integrated surface-groundwater modeling. Previous works indicated that a lateral

46 transport of water strongly controls latent heat flux and the partitioning of

47 evapotranspiration into base soil evaporation and plant transpiration (e.g., Maxwell and



48 Condon 2016; Ji et al. 2017; Fang et al. 2017). This effect of a lateral transport of water
49 on land-atmosphere interactions has been recognized (e.g., Williams and Maxwell 2011;
50 Keune et al. 2016).

51

52 Data assimilation has contributed to improving the performance of LSMs by fusing
53 simulation and observation. The grand challenge of land data assimilation is to improve
54 the simulation of unobservable variables using observations by propagating observations'
55 information into model's high dimensional state and parameter space. In previous works
56 on the conventional 1-D LSMs, many land data assimilation systems (LDASs) have been
57 proposed to accurately estimate model's state and parameter variables, which cannot be
58 directly observed, by assimilating satellite and in-situ observations. For example, the
59 optimization of LSM's unknown parameters (e.g., hydraulic conductivity) has been
60 implemented by assimilating remotely sensed microwave observations (e.g., Yang et al.
61 2007; Yang et al. 2009; Bandara et al. 2014; Bandara et al. 2015; Sawada and Koike 2014;
62 Han et al. 2014). Kumar et al. (2009) focused on the correlation between surface and root-
63 zone soil moistures to examine the potential of assimilating surface soil moisture
64 observations to estimate root-zone soil moisture. Sawada et al. (2015) successfully
65 improved the simulation of root-zone soil moisture by assimilating microwave brightness



66 temperature observations which include the information of vegetation water content.

67 Gravity Recovery and Climate Experiment total water storage observation has been

68 intensively used to improve the simulation of groundwater and soil moisture (e.g., Li et

69 al. 2012; Houborg et al. 2012). Improving the simulation of state variables such as soil

70 moisture and biomass by LDASs has contributed to accurately estimating fluxes such as

71 evapotranspiration (e.g. Martens et al. 2017) and CO₂ flux (e.g., Verbeeck et al. 2011).

72 However, in most of the studies on the conventional 1-D LDASs, observations impacted

73 state variables and parameters only in a single model's horizontal grid which is identical

74 to the location of the observation. The assumption that the water flows are restricted to

75 vertical direction in LSMs makes it difficult to propagate observation's information

76 horizontally. It limits the potential of land data assimilation to fully use land hydrological

77 observations.

78

79 The hyperresolution land models, which explicitly solve surface and subsurface lateral

80 flows, provide a unique opportunity to examine the potential of land data assimilation to

81 propagate observation's information horizontally in a model space and efficiently use land

82 hydrological observations. Previous works successfully applied Ensemble Kalman Filters

83 (EnKF) to 3-D Richards' equation-based integrated surface-groundwater models. For



84 example, Camporese et al. (2009) and Camporese et al. (2010) successfully assimilated
85 synthetic observations of surface pressure head and streamflow into the Catchment
86 Hydrology (CATHY). Ridler et al. (2014) successfully assimilated Soil Moisture and
87 Ocean Salinity satellite-observed surface soil moisture into the MIKE SHE distributed
88 hydrological model (see also Zhang et al. (2015)). Kurtz et al. (2016) coupled the Parallel
89 Data Assimilation Framework (PDAF) (Nerger and Hiller 2013) with the Terrestrial
90 System Modelling Framework (TerrSysMP) (Shrestha et al. 2014) and successfully
91 estimate the spatial distribution of soil moisture and saturated hydraulic conductivity in
92 the synthetic experiment (see also Zhang et al. (2018)). In addition, Kurtz et al. (2016)
93 indicated that their EnKF approach is computationally efficient in high-performance
94 computers. Those studies have significantly contributed to fully assimilating the new
95 high-resolution soil moisture observations such as Sentinel-1 (e.g., Paroschia et al. 2013)
96
97 Although the data assimilation of hydrological observations into hyperresolution land
98 models has been successfully implemented in the synthetic experiments, it is unclear how
99 topography-driven surface lateral water flows matter for data assimilation of soil moisture
100 observations. Previous studies on data assimilation with high resolution models mainly
101 focused on assimilating groundwater observations (e.g., Ait-El-Fquih et al. 2016;



102 Rasmussen et al. 2015; Hendricks-Franssen et al. 2008). There are some applications
103 which focused on the observation of soil moisture and pressure head in shallow
104 unsaturated soil layers. However, in those studies, topography-driven surface flow has
105 not been considered in the experiment (Kurtz et al. 2016) or the role of them in
106 assimilating observations into the hyperresolution land models has not been quantitatively
107 discussed (Camporese et al. 2010; Camporese et al. 2009). This study aims at clarifying
108 if surface lateral flows matter for data assimilation of soil moisture observations into
109 hyperresolution land models by a minimalist numerical experiment.

110

111

112 **2. Methods**

113 **2.1. Model**

114 ParFlow is an open source platform which realizes fully integrated surface-groundwater
115 flow modeling (Kollet and Maxwell 2006; Maxwell et al. 2015). This model can be
116 efficiently parallelized in high performance computers and has been widely used as a core
117 hydrological module in hyperresolution land models (e.g., Maxwell and Kollet 2008;
118 Maxwell and Condon 2016; Fang et al. 2017; Kurtz et al. 2016; Maxwell et al. 2011;
119 Williams and Maxwell 2011; Shrestha et al. 2014). Since I used this widely adopted solver



120 as is and added nothing new to the model physics, I described the method of ParFlow to
121 simulate integrated surface-subsurface water flows briefly and omitted the details of
122 numerical methods. The complete description of ParFlow can be found in Kollet and
123 Maxwell (2006), Maxwell et al. (2015) and references therein.

124

125 In the subsurface, ParFlow solves the variably saturated Richards equation in three
126 dimensions.

127 $S_S S_W(h) \frac{\partial h}{\partial t} + \phi S_W(h) \frac{\partial S_W(h)}{\partial t} = \nabla \cdot \mathbf{q} + q_r \quad (1)$

128 $\mathbf{q} = -\mathbf{K}_s(x) k_r(h) [\nabla(h + z) \cos\theta_x + \sin\theta_x] \quad (2)$

129 In equation (1), h is the pressure head [L]; z is the elevation with the z axis specified as
130 upward [L]; S_S is the specific storage [L^{-1}]; S_W is the relative saturation; ϕ is the
131 porosity [-]; q_r is a source/sink term. Equation (2) describes the flux \mathbf{q}
132 [LT^{-1}] by Darcy's law, and \mathbf{K}_s is the saturated hydraulic conductivity tensor [LT^{-1}]; k_r
133 is the relative permeability [-]; θ is the local angle of topographic slope (see Maxwell et
134 al. 2015). In this paper, the saturated hydraulic conductivity is assumed to be isotropic
135 and a function of z :

136 $\mathbf{K}_s = K_s(z) = K_{s,surface} \exp(-f(z_{surface} - z)) \quad (3)$



137 where $K_{s,surface}$ is the saturated hydraulic conductivity at the surface soil, and $z_{surface}$
138 is the elevation of the soil surface. The saturated hydraulic conductivity decreases
139 exponentially as the soil depth increases (Beven 1982). A van Genuchten relationship
140 (van Genuchten 1980) is used for the relative saturation and permeability functions.

$$141 \quad S_W(h) = \frac{S_{sat} - S_{res}}{(1 + (\alpha h)^n)^{(1 - \frac{1}{n})}} + S_{res} \quad (4)$$

$$142 \quad k_r(h) = \frac{(1 - \frac{(ah)^{n-1}}{(1 + (\alpha h)^n)^{(1 - \frac{1}{n})}})^2}{(1 + (\alpha h)^n)^{\frac{(1 - \frac{1}{n})}{2}}} \quad (5)$$

143 where α [L-1] and n [-] are soil parameters, S_{sat} is the relative saturated water content
144 and S_{res} is the relative residual saturation.

145

146 Overland flow is solved by the two-dimensional kinematic wave equation. The dynamics
147 of the surface ponding depth, h [L], can be described by:

$$148 \quad \mathbf{k} \cdot [-K_s(z)k_r(h) \cdot \nabla(h + z)] = \frac{\partial \|h, 0\|}{\partial t} - \nabla \cdot \|h, 0\| \mathbf{v}_{sw} + q_r \quad (4)$$

149 In equation (4), \mathbf{k} is the unit vector in the vertical and $\|h, 0\|$ indicates the greater value
150 of the two quantities following the notation of Maxwell et al. (2015). This formulation
151 results in the overland flow equation being represented as a boundary condition to the
152 variably saturated Richards equation (Kollet and Maxwell 2006). If $h < 0$, equation (4)
153 describes that vertical fluxes across the land surface is equal to the source/sink term q_r
154 (i.e., rainfall and evapotranspiration). If $h > 0$, the terms on the right-hand side of equation



155 (4), which indicate water fluxes routed according to surface topography, are active. \mathbf{v}_{sw}

156 is the two-dimensional depth-averaged water flow velocity [LT^{-1}] and estimated by the

157 Manning's law:

158
$$\mathbf{v}_{sw,x} = \left(\frac{\sqrt{S_{f,x}}}{n_M} h^2 \right), \mathbf{v}_{sw,y} = \left(\frac{\sqrt{S_{f,y}}}{n_M} h^2 \right) \quad (5)$$

159 where $S_{f,x}$ and $S_{f,y}$ are the friction slopes [-] for the x- and y-direction, respectively;

160 n_M is the Manning's coefficient [$TL^{-1/3}$]. In the kinematic wave approximation, the

161 friction slopes are set to the bed slopes. The methodology of discretization and numerical

162 method to solve equations (1-5) can be found in Kollet and Maxwell (2006).

163

164

165 **2.2. Data Assimilation**

166 In this paper, the ensemble Kalman filter (EnKF) was applied to assimilate soil moisture

167 observations into ParFlow. The EnKF has widely been applied to hyper-resolution land

168 models (e.g., Camporese et al. (2009); Camporese et al. (2010); Ridler et al. (2014);

169 Zhang et al. (2015); Kurtz et al. (2016); Zhang et al. (2018)). I examined if surface lateral

170 flows matter for data assimilation of soil moisture observations into hyperresolution land

171 models using this widely adopted data assimilation method.

172



173 The Parflow model can be formulated as a discrete state-space dynamic system:

174 $\mathbf{x}(t+1) = f(\mathbf{x}(t), \boldsymbol{\theta}, \mathbf{u}(t)) + \mathbf{q}(t)$ (8)

175 where $\mathbf{x}(t)$ is the state variables (i.e. pressure head), $\boldsymbol{\theta}$ is the time-invariant model

176 parameters (i.e. saturated hydraulic conductivity), $\mathbf{u}(t)$ is the external forcing (i.e.,

177 rainfall and evapotranspiration), and $\mathbf{q}(t)$ is the noise process which represents the

178 model error. In data assimilation, it is useful to formulate an observation process as

179 follows:

180 $\mathbf{y}^f(t) = \mathcal{H}(\mathbf{x}(t)) + \mathbf{r}(t)$ (9)

181 where $\mathbf{y}^f(t)$ is the simulated observation, \mathcal{H} is the observation operator which maps

182 the model's state variables into the observable variables, and $\mathbf{r}(t)$ is the noise process

183 which represents the observation error. The purpose of EnKF (and any other data

184 assimilation methods) is to find the optimal state variables $\mathbf{x}(t)$ based on the simulation

185 $\mathbf{y}^f(t)$ and observation (defined as \mathbf{y}^o) considering their errors ($\mathbf{q}(t)$ and $\mathbf{r}(t)$)

186

187 The general description of the Kalman filter is the following:

188 $\mathbf{x}^f(t) = \mathcal{M}[\mathbf{x}^a(t-1)]$ (6)

189 $\mathbf{x}^a(t) = \mathbf{x}^f(t) + \mathbf{K}[\mathbf{y}^o - \mathcal{H}(\mathbf{x}^f(t))]$ (7)

190 $\mathbf{K} = \mathbf{P}^f \mathcal{H}^T (\mathcal{H} \mathbf{P}^f \mathcal{H}^T + \mathbf{R})^{-1}$ (8)



191 $\mathbf{P}^a = (\mathbf{I} - \mathbf{K}\mathbf{H})\mathbf{P}^f$ (9)

192 I follow the notation of Houtekamer and Zhang (2016). Superscripts f and a are forecast

193 and analysis, respectively. In equation (6), a forecast model \mathcal{M} (ParFlow in this study)

194 is used to obtain a prior estimate at time t, $\mathbf{x}^f(t)$, from the estimation at the previous time

195 $\mathbf{x}^a(t-1)$. In equation (7), a prior estimate $\mathbf{x}^f(t)$ is updated to the analysis state, $\mathbf{x}^a(t)$,

196 using new observations \mathbf{y}^0 . The Kalman gain matrix \mathbf{K} , calculated by equation (8), gives

197 an appropriate weight for the observations with an error covariance matrix \mathbf{R} , and the

198 prior with an error covariance matrix \mathbf{P}^f . \mathbf{P}^a is an updated analysis error covariance.

199 To calculate \mathbf{K} , the observation operator \mathbf{H} is needed to map from model space to

200 observation space. It should be noted that the equations (6-9) give an optimal estimation

201 only when the model and observation errors follow the Gaussian distribution. When the

202 probabilistic distribution of the error in either model or observation has a non-Gaussian

203 structure, results of the Kalman filter are suboptimal. This point is important to interpret

204 the results of this study.

205

206 EnKF is the Monte Carlo implementation of equations (6-9). To compute the Kalman gain

207 matrix, \mathbf{K} , ensemble approximations of $\mathbf{P}^f\mathbf{H}^T$ and $\mathbf{H}\mathbf{P}^f\mathbf{H}^T$ can be given by:

208 $\mathbf{P}^f\mathbf{H}^T \equiv \frac{1}{k-1} \sum_{i=1}^k (\mathbf{x}_i^f - \bar{\mathbf{x}}^f) (\mathbf{H}\mathbf{x}_i^f - \bar{\mathbf{H}\mathbf{x}}^f)^T$ (10)



209 $\mathcal{H}P^f\mathcal{H}^T \equiv \frac{1}{k-1} \sum_{i=1}^k (\mathcal{H}\mathbf{x}_i^f - \overline{\mathcal{H}\mathbf{x}^f})(\mathcal{H}\mathbf{x}_i^f - \overline{\mathcal{H}\mathbf{x}^f})^T$ (11)

210 where \mathbf{x}_i^f is the ith member of a k-member ensemble prior and $\overline{\mathbf{x}^f} = \frac{1}{k} \sum_{i=1}^k \mathbf{x}_i^f$ and

211 $\overline{\mathcal{H}\mathbf{x}^f} = \frac{1}{k} \sum_{i=1}^k \mathcal{H}\mathbf{x}_i^f$.

212

213 Once $\overline{\mathbf{x}^a} = \sum_{i=1}^k \mathbf{x}_i^a$ (\mathbf{x}_i^a is the ith member of a k-member ensemble analysis) and $\mathbf{P}^a =$

214 $\frac{1}{k-1} \sum_{i=1}^k (\mathbf{x}_i^a - \overline{\mathbf{x}^a})(\mathbf{x}_i^a - \overline{\mathbf{x}^a})^T$ are computed by equations (6-11), there are many

215 choices of an analysis ensemble. Although equations (6-11) can calculate the mean and

216 variance of the ensemble members, they do not tell how to adjust the state of the ensemble

217 members in order to realize the estimated mean and variance. There are many proposed

218 flavors of EnKF and one of the differences among them is the method to choose the

219 analysis \mathbf{x}_i^a . In this paper, the Ensemble Transform Kalman Filter (ETKF; Bishop et al.

220 2001; Hunt et al. 2007) was used to transport forecast ensembles to analysis ensembles.

221 ETKF has been used for hyperresolution land data assimilation (e.g., Kurtz et al. 2016).

222 Please refer to Hunt et al. (2007) for the complete description of the ETKF and its

223 localized version, the Local Ensemble Transform Kalman Filter (LETKF). The open

224 source available at <https://github.com/takemasa-miyoshi/letkf> was used in this study as

225 the ETKF code library.

226



227 In many ensemble Kalman filter systems, the ensemble spread, \mathbf{P}^a , tends to become too
228 underdispersive to stably perform data assimilation cycles without any ensemble inflation
229 methods (Houtekamer and Zhang, 2016). To overcome this limitation, \mathbf{P}^a is arbitrarily
230 inflated after data assimilation. In this paper, the relaxation to prior perturbation method
231 (RTTP) of Zhang et al. (2004) was used to maintain an appropriate ensemble spread. In
232 the RTTP, the computed analysis perturbations are relaxed back to the forecast
233 perturbations:

234
$$\mathbf{x}_{i,new}^a - \bar{\mathbf{x}}^a = (1 - \alpha)(\mathbf{x}_i^a - \bar{\mathbf{x}}^a) + \alpha(\mathbf{x}_i^f - \bar{\mathbf{x}}^f), \quad 0 \leq \alpha \leq 1 \quad (12)$$

235 where α was set to 0.975 in this study. If $\alpha = 1$, the analysis spread is identical to the
236 background spread. Many studies show that the ensemble inflation works well when α
237 remains fairly close to 1 (see also the comprehensive review by Houtekamer and Zhang
238 2016).

239
240 In the data assimilation experiments, I adjusted pressure head by data assimilation so that
241 \mathbf{x}^f is pressure head. Since the surface saturated hydraulic conductivity was also adjusted,
242 \mathbf{x}^f includes log-transformed $K_{s,surface}$. I assimilated volumetric soil moisture
243 observations so that \mathbf{y}^f and \mathbf{y}^o are simulated and observed volumetric soil moisture,
244 respectively. The van Genuchten relationship converts the adjusted state variables \mathbf{x}^f to



245 the observable variables \mathbf{y}^f and can be recognized as an observation operator \mathcal{H} .

246 However, since volumetric soil moisture \mathbf{y}^f has already been calculated by Parflow, I did
247 not need the van Genuchten relationship in data assimilation.

248

249

250 **2.3. Kullback-Leibler divergence**

251 To evaluate the non-Gaussianity of the background error sampled by an ensemble, I used
252 the Kullback-Leibler divergence (KLD) (Kullback and Leibler 1951):

$$253 D_{KL}(p, q) = \sum_i p(i) \log \frac{p(i)}{q(i)} \quad (13)$$

254 where $D_{KL}(p, q)$ is the KLD between two probabilistic distribution functions (PDFs), p
255 and q . If two PDFs are equal for all i , $D_{KL}(p, q) = 0$. A large value for $D_{KL}(p, q)$
256 indicates that the two PDFs, p and q , substantially differ from each other. Therefore,
257 the KLD can be used as an index to evaluate the closeness of two PDFs. In this study, I
258 compared the PDF of the ensemble simulation (p in equation (13)) with the Gaussian PDF
259 which has the mean and variance of the ensembles (q in equation (13)). A large value for

260 $D_{KL}(p, q)$ indicates the state variables simulated by ensembles do not follow the
261 Gaussian PDF. It should be noted that the KLD is not symmetric ($D_{KL}(p, q) \neq D_{KL}(q, p)$).

262 The KLD has been used to quantitatively evaluate the Gaussianity of the sampled



263 background error in the studies on data assimilation (e.g., Kondo and Miyoshi 2019; Duc
264 and Saito 2018).

265

266

267 **3. Synthetic experiments**

268 In this study, I performed two synthetic experiments. In the synthetic experiments, I
269 generated the synthetic truth of the state variables by driving ParFlow with the specified
270 parameters and input data. Then the synthetic observations were generated by adding the
271 Gaussian white noise to this synthetic truth. The performance of data assimilation was
272 evaluated by comparing the estimated state and parameter values by ETKF with the
273 synthetic truth. This synthetic experiment has been recognized as an important research
274 method to analyze how data assimilation works (e.g., Moradkhani et al. 2005; Camporese
275 et al. 2009; Vrugt et al. 2013; Kurtz et al. (2016); Sawada et al. 2018)

276

277

278 **3.1. Simple 2-D slope with homogeneous hydraulic conductivity**

279 **3.1.1. Experiment Design**



280 The synthetic experiment was implemented to examine how topography-driven surface
281 lateral flows contribute to efficiently propagating observation's information horizontally
282 in the data assimilation of soil moisture observation. Two synthetic reference runs were
283 created by Parflow. The 2-D domain has a horizontal extension of 4000m and a vertical
284 extension of 5m. The domain of the virtual slope was horizontally discretized into 40 grid
285 cells with a size of 100m and vertically discretized into 50 grid cells with a size of 0.10m.
286 The domain has a 25% slope. In two synthetic reference runs, it heavily rains only in the
287 upper half of the slope ($2000m < x < 4000m$). Although this rainfall distribution is
288 unrealistic, the effect of surface lateral flows on data assimilation can clearly be discussed
289 in this simplified problem setting. More realistic rainfall distribution will be used in the
290 next synthetic experiment (see section 3.2). A constant rainfall rate of 50mm/h was
291 applied for 3 hours and then the period with no rainfall and evaporation of 0.075mm/h
292 lasted for 117 hours. This 120-hour rain/no rain cycle was repeatedly applied to the
293 domain. There is no rainfall in the lower half of the slope ($0m < x < 2000m$). The
294 configurations described above were schematically shown in Figure 1a. The parameters
295 of the van Genuchten relationship, alpha and n, were set to $1.5 [m^{-1}]$ and 1.75, respectively.
296 Those values are in the reasonable range estimated by the published literature (e.g.,
297 Ghanbarian-Alavijeh et al. 2010). The porosity, ϕ in equation (1), was set to 0.40. The



298 Manning's coefficient, n_M in equation (5), was set to 5.52×10^{-6} [m^{-1/3}h]. These
299 clayey soil properties described above are applied to the whole domain. The groundwater
300 table was located at z=3m and the hydrostatic pressure gradient was assumed for the
301 initial pressure heads in the unsaturated soil layers.

302

303 The difference between two synthetic reference runs is the value of saturated hydraulic
304 conductivity. The surface saturated hydraulic conductivity, $K_{s,surface}$ in equation (3),
305 was set to 0.005 [m/h] in one reference, and 0.02 [m/h] in the other. These surface
306 saturated hydraulic conductivities described above are applied to the whole domain.

307 Figure 1 shows the difference of the response to heavy rainfall between the two synthetic
308 reference runs. In the case of the low saturated hydraulic conductivity (hereafter called
309 the LOW_K reference), larger surface lateral flows are generated than the case of the high

310 saturated hydraulic conductivity (hereafter called the HIGH_K reference). In the LOW_K
311 reference, the topography-driven surface lateral flows reach the left edge of the domain

312 (Figure 1b). In the HIGH_K reference, supplied water moves vertically rather than
313 horizontally and the topography-driven surface flow reaches around x = 1000~1500m
314 (Figure 1d).

315



316 For the data assimilation experiment, an ensemble of 50 realizations was generated. Each
317 ensemble member has different saturated hydraulic conductivity and rainfall rate.
318 Lognormal multiplicative noise was added to surface saturated hydraulic conductivity
319 and rainfall rate of the synthetic reference runs. This specification of uncertainty in
320 rainfall was also adopted in Crow et al. (2011). The two parameters of the lognormal
321 distribution, commonly called μ and σ , were set to 0 and 0.15, respectively. The initial
322 groundwater depth of each ensemble member was drawn from the uniform distribution
323 from 2.0m to 3.5m. The hydrostatic pressure gradient was assumed for the initial pressure
324 heads in the unsaturated soil layers.

325

326 The virtual hourly observations were generated by adding the Gaussian white noise whose
327 mean is zero to the volumetric soil moisture simulated by the synthetic reference runs.
328 The observation error (the standard deviation of the added Gaussian white noise) was set
329 to $0.05 \text{ m}^3/\text{m}^3$. It was assumed that the volumetric soil moistures can be observed in every
330 model's soil layer from surface to the depth of 1m at the specific location. These soil
331 moisture observations can be obtained in the in-situ observation sites (e.g., Dorigo et al.,
332 2017). In the section 3.2, I will assume that only surface soil moisture observation can be
333 accessed, which is more realistic since satellite sensors can observe only surface soil



334 moisture. I assumed that the small part of the domain can be observed. The two scenarios
335 of the observation's location are provided. In the first scenario (hereafter called the UP_O
336 scenario), the volumetric soil moisture at the upper part of the slope ($x = 2500\text{m}$) was
337 observed. In the UP_O scenario, I could observe the volumetric soil moisture in the upper
338 part of the slope where it heavily rains and tried to infer the soil moisture in the lower part
339 of the slope where it does not rain by propagating the observation's information downhill.
340 In the second scenario (hereafter called the DOWN_O scenario), the volumetric soil
341 moisture at the lower part of the slope ($x = 1500\text{m}$) was observed. In the DOWN_O
342 scenario, I could observe the volumetric soil moisture in the lower part of the slope where
343 it does not rain and tried to infer the soil moisture in the upper part of the slope where it
344 heavily rains by propagating the observation's information uphill.
345
346 Since I had the two synthetic reference runs (the HIGH_K and LOW_K references) and
347 the two observation scenarios (the UP_O and DOWN_O scenarios), I implemented totally
348 four data assimilation experiments. Table 1 summarizes the data assimilation experiments
349 implemented in this study. For instance, in the HIGH_K-UP_O experiment, I chose the
350 HIGH_K reference and generated an ensemble of 50 realizations from the HIGH_K
351 reference. The soil moisture observations were generated from the HIGH_K reference at



352 the location of $x = 2500\text{m}$ and assimilated into the model every hour. The simulated
353 volumetric soil moisture of the data assimilation experiment was compared with that of
354 the HIGH_K reference.

355

356 In addition to the data assimilation (DA) experiments, I implemented the NoDA
357 experiment (also called the open-loop experiment in the literature of the LDAS study) in
358 which the ensemble was used but no observation data were assimilated. Please note that
359 in the NoDA experiment, the true rainfall rate and saturated hydraulic conductivity were
360 unknown so that I could not accurately estimate the synthetic true state variables. I will
361 evaluate how this negative impact of uncertainties in rainfall and saturated hydraulic
362 conductivity can be mitigated by data assimilation in the DA experiment.

363

364 As evaluation metrics, root-mean-square-error (RMSE) was used:

$$365 \text{ RMSE} = \sqrt{\frac{1}{k} \sum_{i=1}^k (F_i - T)^2} \quad (14)$$

366 where k is the ensemble number, F_i is the volumetric soil moisture simulated by the i -th
367 member in the DA or NoDA experiment, T is the volumetric soil moisture simulated by
368 the synthetic reference run.

369



370 To evaluate the impact of data assimilation, the improvement rate (IR) was defined and

371 calculated by the following equation:

372
$$IR = \frac{\overline{RMSE_{DA}} - \overline{RMSE_{NoDA}}}{\overline{RMSE_{NoDA}}} \quad (15)$$

373 where $\overline{RMSE_{DA}}$ and $\overline{RMSE_{NoDA}}$ are time-mean RMSE of the DA and NoDA

374 experiments, respectively. The negative IR indicates that data assimilation positively

375 impacts the simulation of soil moisture. The metrics described above was calculated in

376 the whole domain. In the DA experiment, soil moisture values before the update by ETKF

377 (i.e. initial guess) were used to calculate the metrics.

378

379 Four of 120-hour rain/no rain cycles were applied so that the computation period was 480

380 hours. The spin-up results in the first 120 hours were not used to calculate the evaluation

381 metrics. Since the steady state of groundwater level is not the scope of this paper, the long

382 spin-up is not absolutely necessary.

383

384

385 **3.1.2. Results**

386 Figure 2a shows the IR of the LOW_K-UP_O experiment. The time series of the DA and

387 NoDA experiment and the synthetic reference run in the LOW_K-UP_O experiment can



388 be found in Figure S1. The data assimilation efficiently propagates the information of the
389 observations located in the upper part of the slope (see the black arrow in Figure 2a) both
390 horizontally and vertically. Despite the uncertainty in rainfall and hydraulic conductivity,
391 RMSE is reduced by data assimilation not only directly under the observation but also the
392 lower part of the slope where it does not rain. The estimated $K_{s,surface} \approx 0.00508$ [m/h]
393 by ETKF is mostly identical to the synthetic truth. However, the increase of RMSE by
394 data assimilation can be found at the left edge of the domain, which is far from the location
395 of the observation. The impact of data assimilation on the surface soil moisture simulation
396 is small because the volumetric soil moisture's RMSE of the NoDA experiment in this
397 surface soil layer is already small ($\leq 0.01\text{m}^3/\text{m}^3$) in the case of the LOW_K reference so
398 that any improvements do not make sense.

399

400 Figure 2b shows the IR of the LOW_K-DOWN_O experiment (see also Figure S2 for
401 time series). The IR's spatial pattern of the LOW_K-DOWN_O experiment is similar to
402 that of the LOW_K-UP_O experiment except for the left edge of the domain. It is
403 promising that I can accurately infer soil moisture in the region where it heavily rains
404 from the shallow soil moisture observations in the region where it does not rain. The
405 estimated $K_{s,surface} \approx 0.00512$ [m/h] by ETKF is mostly identical to the synthetic truth.



406

407 Figure 3a shows the difference of time-mean RMSEs (\overline{RMSE}_{DA} in equation (15))
408 between the LOW_K-UP_O and LOW_K-DOWN_O experiments. Although observing
409 the lower part of the slope slightly improves the soil moisture simulation at the left edge
410 of the domain compared with observing the upper part of the slope (the reason for it will
411 be explained later), there are few differences between the UP_O and DOWN_O scenarios
412 in the case of the LOW_K reference. The soil moisture observations have large
413 representativeness and I can efficiently infer soil moisture in the soil columns which are
414 horizontally and vertically far from the observations.

415

416 Figure 2c shows the IR of the HIGH_K-UP_O experiment (see also Figure S3 for time
417 series). The data assimilation significantly reduces RMSE of the soil moisture simulation
418 directly under the observations (see the black arrow in Figure 2c), which indicates that
419 the data assimilation efficiently propagates the information of the observations vertically.
420 The saturated hydraulic conductivity estimated by ETKF is mostly identical to the
421 synthetic truth ($K_{s,surface} \approx 0.0204$ [m/h]). However, the impact of the data assimilation
422 on the soil moisture simulation in the lower part of the slope around x=1500m is marginal
423 although there are large RMSE in the NoDA experiment ($>0.05\text{m}^3/\text{m}^3$) at the edge of the



424 area where topography-driven surface flow reaches in the HIGH_K reference (see Figure

425 1d).

426

427 Figure 2d shows the IR of the HIGH_K-DOWN_O experiment (see also Figure S4 for

428 time series). Although the observations in the lower part of the slope (see the black arrow

429 in Figure 2d) significantly contribute to improving the soil moisture simulation in the

430 downstream area of the observation and accurately estimating $K_{s,surface} \approx 0.0208$

431 [m/h], the impact of the data assimilation on the shallow soil moisture simulation around

432 $x=500\text{--}1000\text{m}$ is marginal. As I found in the LOW_K-DOWN_O experiment, the shallow

433 soil moisture observations in the region where it does not rain can improve the soil

434 moisture simulation in the region where it heavily rains. However, the IR of the HIGH_K-

435 DOWN_O experiment in the upper part of the slope is smaller than that of the LOW_K-

436 DOWN_O experiment (see Figure 2b and 2d).

437

438 The high representativeness of the observations which I found in the case of the LOW_K

439 reference (i.e. the small difference of RMSEs between two observation scenarios) cannot

440 be found in the case of the HIGH_K reference. Figure 3b shows the difference of time-

441 mean RMSEs ($\overline{RMSE_{DA}}$ in equation (15)) between the HIGH_K-UP_O and HIGH_K-



442 DOWN_O experiments. Compared with the LOW_K reference case (Figure 3a), there
443 are significant differences between the UP_O and DOWN_O scenarios in the case of
444 higher saturated hydraulic conductivity. In this case, the vertical propagation of the
445 observations' information is more efficient than the horizontal propagation.

446

447 The relatively low efficiency of the data assimilation and the low representativeness of
448 the soil moisture observations in the case of the HIGH_K reference are caused by the
449 non-Gaussian background error distribution. I calculated KLD by comparing the PDF of
450 the NoDA ensemble (p in equation (13)) with the Gaussian PDF which has the mean and
451 variance of the NoDA ensemble (q in equation (13)). Figure 4 shows that the NoDA
452 ensemble in the case of the HIGH_K reference has stronger non-Gaussianity than the case
453 of the LOW_K reference especially in the shallow soil layers. The strong non-Gaussianity
454 of the NoDA ensemble generated from the HIGH_K reference can be found at the edge
455 of the area where the topography-driven surface flow reaches (Figure 1d). Figure 5 shows
456 that there is the bifurcation of the ensemble in this region when the ensemble is generated
457 from the HIGH_K reference. The process of topography-driven surface flows is switched
458 on if and only if the surface soil is saturated (see equation (4)) so that the ensemble tends
459 to be bifurcated into the members with surface flows and without surface flows. As I



460 mentioned in section 2.2, in the ETKF, the state and parameter variables are adjusted
461 assuming the Gaussian PDF of the model's error and the linear relationship between
462 observed variables and unobserved variables. Therefore, the non-Gaussianity of the prior
463 ensemble induced by the strong non-linear dynamics of surface lateral flows makes the
464 ETKF inefficient. It is more difficult to reconstruct 3-D fields of soil moisture in high
465 conductivity soils since the 1-D vertical water movement is more dominant. The absolute
466 RMSE of the NoDA experiment in the HIGH_K reference is larger than the LOW_K
467 reference in many places (not shown). Please note that the non-Gaussianity can also be
468 found in the LOW_K reference at the edge of the domain (x=500m) due to the non-linear
469 dynamics of surface lateral flows, which causes the degradation of the soil moisture
470 simulation in the LOW_K-UP_O experiment (see Figure 2a).

471
472 One of the major simplifications in this experiment is spatially homogeneous surface
473 saturated hydraulic conductivity. The optimization of it can efficiently improve the soil
474 moisture simulation in the whole domain. However, the optimization of this
475 homogeneous surface saturated hydraulic conductivity has a limited impact on the soil
476 moisture simulation. Figure S5 shows the IR of the HIGH_K-DOWN_O experiment
477 where the parameter optimization by ETKF is switched off. Even if I do not optimize the



478 surface saturated hydraulic conductivity, I could obtain the similar IR to the original
479 experiment and the shallow soil moisture observations in the region where it does not rain
480 can improve the soil moisture simulation in the region where it heavily rains. The
481 horizontal propagation of the observations' information shown in this experiment was
482 brought out not only by the estimation of spatially homogeneous saturated hydraulic
483 conductivity but also by the adjustment of state variables (i.e., pressure head and
484 volumetric soil moisture).

485

486 Please note that the improvement of the soil moisture simulation cannot be found if the
487 topography-driven surface flow is neglected. Figure S6 shows the IR of the LOW-
488 K_DOWN-O experiment where the topography-driven surface flow is neglected in the
489 ParFlow simulation. Please note that although many conventional land surface models
490 neglected or parameterized lateral flows, this assumption can be applied only in the coarse
491 spatial resolution (>25km), which is not the case of this experimental setting. The
492 imperfect model physics of ParFlow substantially degrades the skill to simulate soil
493 moisture and data assimilation cannot compensate this degradation. This point will also
494 be discussed in the section 3.2 more deeply.

495



496 **3.2. Simple 3-D slope with heterogeneous hydraulic conductivity**

497 **3.2.1. Experiment design**

498 To further demonstrate how land data assimilation works with topography-driven surface
499 lateral flows, I implemented another synthetic experiment which is more realistic than
500 that shown in section 3.1. The 3-D domain has a horizontal extension of 4000 m×4000m
501 and a vertical extension of 3m. The domain was horizontally discretized into 40×40 grid
502 cells with a size of 100m×100m and vertically discretized into 30 grid cells with a size
503 of 0.1m. The domain has a 10% slope in both x and y directions (see Figure 6a). The
504 parameters of the van Genuchten relationship, porosity and Manning's coefficient were
505 set to the same variables for the synthetic experiment in section 3.1.

506

507 The spatially heterogeneous surface saturated hydraulic conductivity was generated
508 following Kurtz et al. (2016). The field of $\log_{10}(K_{s,surface})$ was generated by two-
509 dimensional unconditioned sequential Gaussian simulation. A Gaussian variogram with
510 nugget, sill, and range values of 0.0 $\log_{10}(\text{m/h})$, 0.1 $\log_{10}(\text{m}^2\text{h}^2)$, and 12 model
511 grids (1200m), respectively was used to simulate the spatial distribution of
512 $\log_{10}(K_{s,surface})$. A constant value of -2.30 $\log_{10}(\text{m/h})$ (i.e. 0.005 (m/h)) was added
513 to the generated field so that the mean of the logarithm of surface saturated hydraulic



514 conductivity was set to -2.30 (i.e. 0.005(m/h)). This method to generate the field of the
515 saturated hydraulic conductivity has been used previously (e.g., Kurtz et al. 2016).
516 Subsurface saturated hydraulic conductivity was calculated by equation (3). An ensemble
517 of 51 realizations of $\log_{10}(K_{s,surface})$ was generated and one of them was chosen as a
518 synthetic reference (Figure 6a). The remaining 50 members were used for data
519 assimilation experiments.

520

521 A rainfall rate $R(x,y)$ (mm/h) was modelled by a logistic function:

$$522 R(x,y) = \frac{R_{max}}{1+100\exp(-0.2 \times \frac{x+y}{2})} \quad (16)$$

523 where x and y are horizontal grid numbers ($1 \leq x \leq 40, 1 \leq y \leq 40$). In the synthetic
524 reference, the maximum rainfall rate in the domain, R_{max} , was set to 50 (mm/h) (Figure
525 6b). This rainfall rate was applied for 3 hours and then the period with no rainfall and
526 evaporation of 0.075mm/h lasted for 117 hours. For data assimilation experiment, an
527 ensemble of 50 realization of $R(x,y)$ was generated by adding a lognormal
528 multiplicative noise to R_{max} of the synthetic reference. The two parameters of the
529 lognormal distribution, commonly called μ and σ , were set to 0 and 0.15, respectively.

530



531 Figure 6c shows the distribution of surface soil moisture in the synthetic reference run.

532 Strong rainfall rate applied in the upper part of the slope generates the topography-driven

533 surface lateral flows. The virtual hourly observations were generated by adding the

534 Gaussian white noise, whose mean is zero and standard deviation is $0.05 \text{ m}^3/\text{m}^3$, to the

535 volumetric surface soil moisture simulated by the synthetic reference run. Unlike the

536 experiment in section 3.1, only surface soil moisture can be observed in this synthetic

537 experiment, which makes this experiment more realistic since satellite sensors can

538 observe only surface soil moisture. Three different observing networks with different

539 observation densities were used (Figure 7). The observing networks shown in Figure 7a,

540 7b, and 7c have totally 1, 9, and 361 observations and are called obs1, obs9, and obs361,

541 respectively.

542

543 In the DA experiments, those virtual observations of surface soil moisture were

544 assimilated every hour to adjust pressure head and saturated hydraulic conductivity. As I

545 did in the section 3.1, the NoDA experiments were also implemented. The two different

546 configurations of ParFlow were used for both DA and NoDA experiments. In the first

547 configuration, called OF (Overland Flow), Parflow explicitly solves overland flows. In

548 the second configuration, called noOF, Parflow assumes the flat terrain for surface flows



549 so that no overland flows are generated. Since the synthetic reference run explicitly
550 considers the topography-driven surface flow, the configuration of noOF assumes that the
551 model physics is imperfect. I implemented 8 numerical experiments which are
552 summarized in Table 2. For example, the OF_DA_obs9 experiment is the data
553 assimilation experiment with the observing network shown in Figure 7b, in which
554 Parflow explicitly solves the topography-driven surface flow. The noOF_NoDA is the
555 model run without assimilating observations, in which Parflow does not consider the
556 topography-driven surface flow.

557

558

559 **3.2.2. Results**

560 Figure 8a shows the RMSE of soil moisture simulation of a second soil layer (i.e. 10-
561 20cm soil depth) in all 8 experiments (the same conclusion described below can be
562 obtained by analyzing all of shallow soil layers). When Parflow explicitly solves the
563 topography-driven surface flow, data assimilation substantially reduces RMSE of the soil
564 moisture simulation (green bars in Figure 8a). The OF_DA_obs361 experiment has the
565 smallest RMSE so that a denser observing network is beneficial to estimate soil moisture.
566 Figure 8b shows the RMSE of the estimation of saturated surface hydraulic conductivity



567 in all 8 experiments. Data assimilation also reduces the uncertainty in model's parameters
568 (green bars in Figure 8b). However, the OF_DA_obs361 experiment has larger RMSE
569 than the other DA experiments. This is because the adjustment of hydraulic conductivity
570 in the OF_DA_obs361 experiment greatly mitigates not only the errors induced by
571 uncertainty in hydraulic conductivity but those induced by uncertainty in rainfall rate. In
572 the OF configuration, there are two sources of errors, rainfall rate and hydraulic
573 conductivity. However, data assimilation can adjust only hydraulic conductivity in this
574 study. Although it is expected that the adjustment of hydraulic conductivity mainly
575 mitigates the errors of simulated volumetric soil moisture induced by uncertainty in
576 hydraulic conductivity, it also greatly mitigates those induced by uncertainty in rainfall
577 rate by adjusting the parameter in the incorrect direction when the number of observations
578 is large. Therefore, the assimilation of a large number of observations degrades the
579 estimation of saturated hydraulic conductivity despite the improvement of the soil
580 moisture simulation.

581

582 The noOF_NoDA experiment has larger RMSE than the OF_NoDA experiment due to
583 the negligence of the topography-driven surface flow. In the noOF configuration, data
584 assimilation also improves the soil moisture simulation (red bars in Figure 8a). The



585 noOF_DA_obs361 experiment outperforms the OF_NoDA experiment so that data
586 assimilation with a dense observing network can compensate the negative impact of
587 neglecting the topography-driven surface flow. Although data assimilation positively
588 impacts the parameter estimation, the denser observing network cannot reduce RMSE of
589 hydraulic conductivity estimation (red bars in Figure 8b). The negative impact of the
590 dense observations in the noOF_DA_obs361 experiment on the parameter estimation is
591 larger than in the OF_DA_obs361 experiment. In addition to rainfall rate and hydraulic
592 conductivity, the imperfect model physics (i.e., no topography-driven surface flow) is the
593 source of error in the noOF configuration. The assimilation of a large number of
594 observations degrades the estimation of saturated hydraulic conductivity because it
595 greatly mitigates the impact of all systematic errors which comes from three different
596 sources only by adjusting hydraulic conductivity.

597

598 Figure 9 shows the difference of RMSE of the soil moisture simulation between the DA
599 experiments and the OF_NoDA experiment. In the DA configuration, the improvement
600 of the soil moisture estimation can be found in a large area even if there is a single
601 observation in the center of the domain (Figure 9a). Figure 9b shows that the increase of
602 the number of observations substantially improves the soil moisture simulation in the



603 region which is affected by topography-driven surface flow (see also Figure 6c). However,
604 the skill to simulate soil moisture is severely degraded in the lower-left corner of the
605 domain, which causes the stalled improvement from the OF_DA_obs1 experiment to the
606 OF_DA_obs9 experiment shown in Figure 8a. Figure 9c shows that although the far
607 denser observing network can slightly mitigate this degradation, increasing the number
608 of observations cannot efficiently solve this issue. This degradation is caused by the
609 bifurcation of ensemble members at the edge of the area where topography-driven surface
610 flow reaches (Figure S7). Figure 10 shows KLD in the OF_NoDA and noOF_NoDA
611 experiments. Figure 10a clearly shows that the ensemble simulation of volumetric soil
612 moisture generates the strong non-Gaussianity at the edge of the area where topography-
613 driven surface flow reaches, which harms the efficiency of the ETKF. This finding is
614 consistent to what I found in the previous experiment in section 3.1.

615

616 In the noOF configuration, there are large errors in the area around $500 \leq x, y \leq 1500$
617 since the increase of soil moisture in this area is caused by the topography-driven surface
618 flow which is neglected in the noOF configuration. Figures 9d and 9e show that the sparse
619 observations cannot completely remove this degradation caused by imperfect model
620 physics. Figure 9f shows that the noOF_DA_obs361 can outperform the OF_NoDA



621 experiment in exchange for the degradation of the parameter estimation as I found in
622 Figure 8. The unstable behavior of the ETKF found in the OF configuration does not
623 occur when the topography-driven surface flow is neglected since the ensemble
624 simulation does not generate the non-Gaussian background distribution (Figure 10b).
625 Although ETKF can significantly improve the simulation skill of the hyperresolution land
626 model in many cases, I found its limitation when it is applied to the problems with the
627 topography-driven surface lateral flows. Figure 10 clearly indicates that this limitation
628 appears only if lateral water flows are explicitly considered.

629

630

631

632 **4. Discussion**

633 In this study, I revealed that the hyperresolution integrated surface-subsurface
634 hydrological model gives the unique opportunity to effectively use soil moisture
635 observations to improve the soil moisture simulation in terms of a horizontal propagation
636 of observation's information in a model space. I found that the explicit calculation of the
637 topography-driven surface flow has an important role in propagating the information of
638 soil moisture observation horizontally by data assimilation even if there is considerable



639 heterogeneity of meteorological forcing. It is possible that the soil moisture observations
640 in the area where it does not heavily rain can improve the soil moisture simulation in the
641 severe rainfall area.

642

643 This potential cannot be brought out in the conventional 1-D LSM where sub-grid scale
644 surface runoff is parameterized and the surface flows in one grid do not move to the
645 adjacent grids. I found that neglecting the topography-driven surface flow causes
646 significant bias in the soil moisture simulation and this bias cannot be completely
647 mitigated by data assimilation especially in the case of a sparse observing network.

648 However, I found that even if the model uses imperfect physics which neglects the
649 interaction between topography-driven surface lateral flows and subsurface soil moisture,
650 assimilating soil moisture observations into the model's three-dimensional state and
651 parameter space can improve the skill to estimate soil moisture and hydraulic conductivity.

652 This finding implies that the conventional 1-D LSM with full 3-D data assimilation may
653 be a computationally cheap and reasonable choice in some cases although many land data
654 assimilation systems with the conventional 1-D LSM currently update state variables only
655 in a single model's horizontal grid which is identical to the location of the observation.

656



657 The conventional ensemble data assimilation (i.e. ETKF) severely suffers from the non-
658 Gaussian background error PDFs caused by the strongly nonlinear dynamics of the
659 topography-driven surface flow although it has been widely used by previous studies (e.g.,
660 Camporese et al. (2009); Camporese et al. (2010); Ridler et al. (2014); Zhang et al. (2015);
661 Kurtz et al. (2016); Zhang et al. (2018)). The efficiency of ETKF to propagate the
662 information of observations horizontally in the model space is limited in the edge of the
663 area where the topography-driven surface flow reaches. Please note that the low
664 representativeness of the soil moisture observations in the case of the HIGH_K reference
665 shown in section 3.1 is due to the core assumption of the Kalman filter that the error PDFs
666 follow the Gaussian distribution so that the increase of the ensemble size cannot solve
667 this issue. I implemented the data assimilation experiment in the case of the HIGH_K
668 reference with an ensemble size of 500, which is 10 times larger than the original
669 experiments shown in section 3.1, and found no significant improvement of the soil
670 moisture simulation (not shown). Some studies revealed that volumetric soil moisture
671 distributions follow the Gaussian distribution better than pressure head so that they
672 recommend to update soil moisture as a state variable (e.g., Zhang et al. (2018)). However,
673 in this study, I found that volumetric soil moisture distributions have bimodal structure



674 and do not follow the Gaussian distribution. The limitation of ensemble Kalman filters

675 found in this study does not depend on the updated state variables.

676

677 The spatially dense soil moisture observations are needed to efficiently constrain state

678 variables at the edge of surface flows. High resolution soil moisture remote sensing based

679 on satellite active and passive combined microwave observations at the 1 km spatial

680 resolution (e.g., He et al. 2018) and the assimilation of those data (Lievens et al. 2017)

681 may be important in the era of the hyperresolution land modeling. High resolution

682 observations of surface inundated water from satellite imagery with a spatial resolution

683 finer than 100 m (e.g., Sakamoto et al. 2007; Arnesen et al. 2013) may also be useful.

684 However, the numerical experiment in section 3.2 implies that the dense observing

685 network of surface soil moisture cannot completely remove the negative impact of the

686 non-Gaussian background PDF.

687

688 Since there is a nonlinear relationship between observed and unobserved variables

689 sampled by an ensemble, a localization method, which spatially restricts the impact of

690 assimilating observations, is crucially needed for real-world applications. In this study,

691 assimilating observation impacted everywhere in the computational domain. If the



692 localization method is applied, assimilating observation influences state variables of the
693 model grids which are near to the location of assimilated observations. The results of this
694 study imply that the optimal localization radius strongly depends on the model parameter
695 (i.e. saturated hydraulic conductivity). Rasmussen et al. (2015) successfully applied the
696 adaptive localization method (Anderson 2007; Bishop and Hodyss 2009) to the data
697 assimilation of groundwater observations into a hydrological model. It is appropriate to
698 adaptively determine the localization radius considering the lack of prior knowledge of
699 how soil moisture simulated by an ensemble is horizontally correlated.

700

701 Reducing the uncertainty in rainfall positively impacts the efficiency of data assimilation
702 since the bifurcation of simulated soil moisture found in Figure 5c is originally induced
703 by the uncertainty in rainfall. Although assimilating land hydrological observations to
704 improve the rainfall input has been intensively investigated (e.g., Sawada et al. 2018;
705 Herrnegger et al. 2015; Crow et al. 2011; Vrugt et al. 2008), it has yet to be applied to
706 hyperresolution land models. Please note that the parameters of the lognormal distribution
707 to model the uncertainty in rainfall were specified to make the rainfall PDF similar to the
708 Gaussian distribution. I chose the lognormal distribution in order not to generate negative
709 rainfall values and I intended not to introduce non-Gaussianity into the external forcing.



710 The rainfall input which follows the Gaussian PDF was transformed into the non-
711 Gaussian PDF of the background error by the strongly nonlinear dynamics of the
712 topography-driven surface flow.

713

714 To explicitly consider non-Gaussianity and non-linear relationship between observed and
715 unobserved variables induced by the topography-driven surface flow, the particle filters
716 may be useful. The particle filter can represent a probability distribution (including non-
717 Gaussian distributions) directly by an ensemble. Particle filters have been intensively
718 applied to conventional 1-D LSMs (e.g., Sawada et al. 2015; Qin et al. 2009) and lumped
719 hydrological models (e.g., Yan and Moradkhani 2016; Vrugt et al. 2013). Although
720 particle filtering in a high dimensional system suffers from the “curse of dimensionality”
721 (e.g., Snyder et al. 2008), some studies developed the methodology to improve the
722 efficiency of particle filtering (e.g., van Leeuwen 2009; Poterjoy et al. 2019). The
723 applicability of particle filtering to 3-D hyperresolution land models should be assessed
724 in the future.

725

726 Since the synthetic numerical experiments in this paper adopted the simple and
727 minimalistic setting, the findings of this paper may be exaggerated. There are no river



728 channels in the synthetic experiment so that the skill to simulate river water level and
729 discharge cannot be discussed, which is the major limitation of this study. The simple
730 representation of soil properties is also a limitation of this study. In future work, the
731 contributions of the topography-driven surface runoff process to the data assimilation of
732 hydrological observations should be quantified in real-world applications. In addition, in
733 the virtual experiment of this paper, I neglected some of the important land processes such
734 as transpiration, canopy interception, snow, and frozen soil. These processes affect the
735 source term of equation (1) in hyper-resolution land models (e.g., Shrestha et al. 2014).
736 Since the inclusion of the neglected processes do not change the structure of the original
737 ParFlow, the findings of this study can be robust to the models which include these
738 processes. Although they are generally not primary factors in the propagation of overland
739 flows generated by extreme rainfall, which has a shorter timescale than the neglected
740 processes, those processes should be considered in the future.

741

742 The other limitation of this study is that I could not thoroughly evaluate the skill of the
743 ensemble data assimilation to quantify the uncertainty of its prediction. Following
744 Abbaszadeh et al. (2019), I calculated the 95% exceedance ratio and found that the
745 ensemble forecast was systematically overconfident (not shown). In the synthetic



746 experiments of this study, the number of rainfall events was small, and the timing and
747 magnitude of rainfall were not diversified. Due to this limited amount of data, it is difficult
748 to deeply discuss the accuracy of the quantified uncertainty by data assimilation. While
749 the skill of lumped hydrological models was often evaluated by the probabilistic
750 performance measures such as the 95% exceedance ratio (e.g., Abbazadeh et al. (2019)),
751 the uncertainty quantification of the simulation of hyper-resolution land models is in its
752 infancy. How surface lateral flows affect the accuracy of the uncertainty quantification by
753 data assimilation should be investigated using more realistic data.

754

755

756 **5. Conclusions**

757 The simplified synthetic experiments of this study indicate that topography-driven lateral
758 surface flows induced by heavy rainfalls do matter for data assimilation of hydrological
759 observations into hyperresolution land models. Even if there is extreme heterogeneity of
760 rainfall, the information of soil moisture observations can be propagated horizontally in
761 the model space and the soil moisture simulation can be improved by the ensemble
762 Kalman filter. However, the nonlinear dynamics of the topography-driven surface flow
763 induces the non-Gaussianity of the model error, which harms the efficiency of data



764 assimilation of soil moisture observations. It is difficult to efficiently constrain model
765 states at the edge of the area where the topography-driven surface flow reaches by linear-
766 Gaussian filters, which brings the new challenge in land data assimilation for
767 hyperresolution land models. Future work will focus on the real-world applications using
768 intense in-situ soil moisture observation networks and/or high-resolution satellite soil
769 moisture observations.

770

771

772 **Acknowledgement**

773 This study was supported by the JSPS KAKENHI grant JP17K18352 and JP18H03800.

774

775 **Code/Data Availability**

776 All data used in this paper are stored in the repository of the University of Tokyo for 5
777 years and available upon request to the author. The ETKF code used in this study can be
778 found at <https://github.com/takemasa-miyoshi/letkf>.

779



780 **Author Contribution**

781 YS designed the study, executed numerical experiments, analyzed the results, and wrote
782 the paper.

783

784 **Competing interests**

785 The author declares no competing interests.

786

787 **References**

788

789 Abbaszadeh, P., Moradkhani, H., and Daescu, D., N.: The Quest for Model Uncertainty
790 Quantification: A Hybrid Ensemble and Variational Data Assimilation Framework. *Water
791 Resources Research*, 55, 2407–2431. <https://doi.org/10.1029/2018WR023629>, 2019.

792

793 Ait-El-Fquih, B., El Gharamti, M., and Hoteit, I.: A Bayesian consistent dual ensemble
794 Kalman filter for state-parameter estimation in subsurface hydrology. *Hydrology and
795 Earth System Sciences*, 20(8), 3289–3307. <https://doi.org/10.5194/hess-20-3289-2016>,

796 2016

797



798 Amesen et al.: Monitoring flood extent in the lower Amazon River floodplain using

799 ALOS/PALSAR ScanSAR images. *Remote Sensing of Environment*, 130, 51-61.

800 <https://doi.org/10.1016/j.rse.2012.10.035>, 2013

801

802 Anderson, J. L.: Exploring the need for localization in ensemble data assimilation using

803 a hierarchical ensemble filter. *Physica D: Nonlinear Phenomena*, 230(1–2), 99–111.

804 <https://doi.org/10.1016/j.physd.2006.02.011>, 2007

805

806 Bandara, R., Walker, J. P., and Rüdiger, C.: Towards soil property retrieval from space:

807 Proof of concept using in situ observations. *Journal of Hydrology*, 512, 27–38.

808 <https://doi.org/10.1016/j.jhydrol.2014.02.031>, 2014

809

810 Bandara, R., Walker, J. P., Rüdiger, C., and Merlin, O.: Towards soil property retrieval

811 from space: An application with disaggregated satellite observations. *Journal of*

812 *Hydrology*, 522, 582-593, <https://doi.org/10.1016/j.jhydrol.2015.01.018>, 2015

813

814 Beven, K.: On subsurface stormflow: an analysis of response times, *Hydrological Science*

815 *Journal*, 27, 505-521, doi:10.1080/02626668209491129, 1982



816

817 Bishop, C.H., Etherton, B., J., and Majumdar, S., J.: Adaptive Sampling with the
818 Ensemble Transform Kalman Filter. Part I: Theoretical Aspects. *Monthly Weather*
819 *Review*, **129**, 420–436, [https://doi.org/10.1175/1520-0493\(2001\)129<0420:ASWTET>2.0.CO;2](https://doi.org/10.1175/1520-0493(2001)129<0420:ASWTET>2.0.CO;2), 2001.

821

822 Bishop, C. H., and Hodyss, D.: Ensemble covariances adaptively localized with ECO-
823 RAP. Part 1: Tests on simple error models. *Tellus*, **61A**, 84–96,
824 <https://doi.org/10.1111/j.1600-0870.2008.00371.x>, 2009.

825

826 Camporese, M., Paniconi, C., Putti, M., and Salandin, P.: Ensemble Kalman filter data
827 assimilation for a process-based catchment scale model of surface and subsurface flow.
828 *Water Resources Research*, **45**(10), 1–14. <https://doi.org/10.1029/2008WR007031>, 2009.

829

830 Camporese, M., Paniconi, C., Putti, M., and Orlandini, S.: Surface-subsurface flow
831 modeling with path-based runoff routing, boundary condition-based coupling, and
832 assimilation of multisource observation data. *Water Resources Research*, **46**(2).
833 <https://doi.org/10.1029/2008WR007536>, 2010.



834

835 Crow, W. T., Van Den Berg, M. J., Huffman, G. J., and Pellarin, T.: Correcting rainfall
836 using satellite-based surface soil moisture retrievals: The Soil Moisture Analysis Rainfall
837 Tool (SMART). *Water Resources Research*, 47(8), 1–15.
838 <https://doi.org/10.1029/2011WR010576>, 2011.

839

840 Dorigo et al.: ESA CCI Soil Moisture for improved Earth system understanding: State-
841 of-the art and future directions, *Remote Sensing of Environment*, 203, 185-215,
842 <https://doi.org/10.1016/j.rse.2017.07.001>, 2017

843

844 Duc, L., and Saito, K.: Verification in the presence of observation errors: Bayesian point
845 of view. *Q. J. R. Meteorol. Soc.*, 144, 1063– 1090. <https://doi.org/10.1002/qj.3275>, 2018.

846

847 Fang, Y., L. R. Leung, Z. Duan, M. S. Wigmosta, R. M. Maxwell, J. Q. Chambers, and J.
848 Tomasella: Influence of landscape heterogeneity on water available to tropical forests in
849 an Amazonian catchment and implications for modeling drought response, *J. Geophys.*
850 *Res. Atmos.*, 122, <https://doi.org/10.1002/2017JD027066>, 2017.

851



852 Ghanbarian-Alavijeh, B., Liaghat, A., Huang, G., H., and van Genuchten, M. Th.,:
853 Estimation of the van Genuchten soil water retention properties from soil textural data.
854 *Pedosphere*. 20(4): 456–465., 2010
855
856 Han, X., Franssen, H.-J. H., Montzka, C. and Vereecken, H.: Soil moisture and soil
857 properties estimation in the Community Land Model with synthetic brightness
858 temperature observations, *Water Resources Research*, 50, 6081 - 6105,
859 <https://doi.org/10.1002/2013WR014586>, 2014
860
861 Herrnegger, M., Nachtnebel, H. P., and Schulz, K.: From runoff to rainfall: inverse
862 rainfall – runoff modelling in a high temporal resolution, 4619–4639.
863 <https://doi.org/10.5194/hess-19-4619-2015>, 2015
864
865 He, L., Hong, Y., Wu, X., Ye, N., Walker, J. P. and Chen, X.: Investigation of SMAP
866 Active–Passive Downscaling Algorithms Using Combined Sentinel-1 SAR and SMAP
867 Radiometer Data. *IEEE Transactions on Geosciences and Remote Sensing*, 56, 4906–
868 4918, <https://doi.org/10.1109/TGRS.2018.2842153>, 2018
869



870 Hendricks Franssen, H. J., and Kinzelbach, W.: Real-time groundwater flow modeling
871 with the Ensemble Kalman Filter: Joint estimation of states and parameters and the filter
872 inbreeding problem. *Water Resources Research*, 44(9), 1–21.
873 <https://doi.org/10.1029/2007WR006505>, 2008
874
875 Houborg, R., Rodell, M., Li, B., Reichle, R., and Zaitchik, B. F.: Drought indicators based
876 on model-assimilated Gravity Recovery and Climate Experiment (GRACE) terrestrial
877 water storage observations. *Water Resources Research*, 48(7).
878 <https://doi.org/10.1029/2011WR011291>, 2012
879
880 Houtekamer, P. L., and Zhang, F.: Review of the Ensemble Kalman Filter for Atmospheric
881 Data Assimilation. *Monthly Weather Review*, MWR-D-15-0440.1.
882 <https://doi.org/10.1175/MWR-D-15-0440.1>, 2016
883
884 Hunt, B. R., Kostelich, E. J., and Szunyogh, I.: Efficient data assimilation for
885 spatiotemporal chaos: A local ensemble transform Kalman filter. *Physica D: Nonlinear
886 Phenomena*, 230(1–2), 112–126. <https://doi.org/10.1016/j.physd.2006.11.008>, 2007
887



888 Ji, P., Yuan, X., and Liang, X. Z.: Do Lateral Flows Matter for the Hyperresolution Land
889 Surface Modeling? *Journal of Geophysical Research: Atmospheres*, 1–16.
890 <https://doi.org/10.1002/2017JD027366>, 2017

891

892 Keune, J., F. Gasper, K. Goergen, A. Hense, P. Shrestha, M. Sulis, and S. Kollet: Studying
893 the influence of groundwater representations on land surface-atmosphere feedbacks
894 during the European heat wave in 2003, *Journal of Geophysical Research. Atmospheres*,
895 121, 13,301–13,325, <https://doi.org/10.1002/2016JD025426>, 2016.

896

897 Kollet, S. J., and Maxwell, R. M.: Integrated surface–groundwater flow modeling: A free-
898 surface overland flow boundary condition in a parallel groundwater flow model.
899 *Advances in Water Resources*, 29(7), 945–958.
900 <https://doi.org/10.1016/j.advwatres.2005.08.006>, 2006.

901

902 Kondo, K., and Miyoshi, T.: Non-Gaussian statistics in global atmospheric dynamics: a
903 study with a 10 240-member ensemble Kalman filter using an intermediate atmospheric
904 general circulation model. *Nonlinear Processes in Geophysics*, 26, 211-225.
905 <https://doi.org/10.5194/npg-26-211-2019>, 2019



906

907 Kumar, S. V., Reichle, R. H., Koster, R. D., Crow, W. T., and Peters-Lidard, C. D.: Role
908 of Subsurface Physics in the Assimilation of Surface Soil Moisture Observations. *Journal*
909 *of Hydrometeorology*, 10(6), 1534–1547. <https://doi.org/10.1175/2009JHM1134.1>, 2009

910

911 Kurtz, W., He, G., Kollet, S. J., Maxwell, R. M., Vereecken, H., and Franssen, H. J. H.:
912 TerrSysMP-PDAF (version 1.0): A modular high-performance data assimilation
913 framework for an integrated land surface-subsurface model. *Geoscientific Model*
914 *Development*, 9(4), 1341–1360. <https://doi.org/10.5194/gmd-9-1341-2016>, 2016.

915

916 Kullback, S., and Leibler, R. A.: On information and sufficiency, *The Annals of*
917 *Mathematical Statistics*, 22, 79-86, 1951.

918

919 Lawrence, D. M., et al.: Parameterization improvements and functional and structural
920 advances in Version 4 of the Community Land Model. *Journal of Advances in Modeling*
921 *Earth Systems*, 3(3), 1–27. <https://doi.org/10.1029/2011MS000045>, 2011

922



923 Li, B., Rodell, M., Zaitchik, B. F., Reichle, R. H., Koster, R. D., and van Dam, T. M.:
924 Assimilation of GRACE terrestrial water storage into a land surface model: Evaluation
925 and potential value for drought monitoring in western and central Europe. *Journal of*
926 *Hydrology*, 446–447, 103–115. <https://doi.org/10.1016/j.jhydrol.2012.04.035>, 2012
927
928 Lievens, et al.: Joint Sentinel-1 and SMAP data assimilation to improve soil moisture
929 estimates. *Geophysical Research Letters*, 44(12), 6145–6153.
930 <https://doi.org/10.1002/2017GL073904>, 2017.
931
932 Martens, B., Miralles, D. G., Lievens, H., Schalie, R. Van Der, and Jeu, R. A. M. De.:
933 GLEAM v3 : satellite-based land evaporation and root-zone soil moisture, *Geoscientific
934 Model Development*, 10, 1903–1925. <https://doi.org/10.5194/gmd-10-1903-2017>, 2017
935
936 Maxwell, R. M., and N. L. Miller: Development of a Coupled Land Surface and
937 Groundwater Model. *Journal of Hydrometeorology*, 6, 233-247.
938 <https://doi.org/10.1175/JHM422.1>, 2005
939



940 Maxwell, R. M., and Condon, L. E.: Connections between groundwater flow and
941 transpiration partitioning. *Science*, 353, 377-380, <https://doi.org/10.1126/science.aaf7891>,
942 2016

943

944 Maxwell, R. M., Condon, L. E., and Kollet, S. J.: A high-resolution simulation of
945 groundwater and surface water over most of the continental US with the integrated
946 hydrologic model ParFlow v3, 923–937. <https://doi.org/10.5194/gmd-8-923-2015>, 2015.

947

948 Maxwell, R. M., and Kollet, S. J.: Interdependence of groundwater dynamics and land-
949 energy feedbacks under climate change, *Nature Geoscience*, 1, 665–669.
950 <https://doi.org/10.1038/ngeo315>, 2008.

951

952 Maxwell, R. M., Lundquist, J. K., Mirocha, J. D., Smith, S. G., Woodward, C. S., and
953 Tompson, A. F. B.: Development of a Coupled Groundwater–Atmosphere Model.
954 *Monthly Weather Review*, 139(1), 96–116. <https://doi.org/10.1175/2010MWR3392.1>,
955 2011

956



957 Moradkhani, H., Hsu, K. L., Gupta, H., and Sorooshian, S.: Uncertainty assessment of
958 hydrologic model states and parameters: Sequential data assimilation using the particle
959 filter. *Water Resources Research*, 41(5), 1–17. <https://doi.org/10.1029/2004WR003604>,
960 2005

961

962 Nerger, L., and Hiller, W.,: Software for ensemble-based data assimilation systems –
963 implementation strategies and scalability. *Computers and Geosciences*. 55, 110–118.
964 <https://doi.org/10.1016/j.cageo.2012.03.026>, 2013

965

966 Niu, G. Y., Paniconi, C., Troch, P. a., Scott, R. L., Durcik, M., Zeng, X., and Goodrich, D.
967 .: An integrated modelling framework of catchment-scale ecohydrological processes: 1.
968 Model description and tests over an energy-limited watershed. *Ecohydrology*, 7(2), 427–
969 439. <https://doi.org/10.1002/eco.1362>, 2014

970

971 Paloscia, S., Pettinato, S., Santi, E., Notarnicola, C., Pasolli, L., and Reppucci, A.: Soil
972 moisture mapping using Sentinel-1 images: Algorithm and preliminary validation.
973 *Remote Sensing of Environment*, 134, 234-248. <https://doi.org/10.1016/j.rse.2013.02.027>,
974 2013.



975

976 Pokhrel, P., and Gupta, H. V.: On the use of spatial regularization strategies to improve
977 calibration of distributed watershed models. *Water Resources Research*, 46(1), 1–17.

978 <https://doi.org/10.1029/2009WR008066>, 2010

979

980 Poterjoy, J., Wicker, L., and Buehner, M.: Progress toward the application of a localized
981 particle filter for numerical weather prediction. *Monthly Weather Review*, 147(4), 1107–
982 1126. <https://doi.org/10.1175/MWR-D-17-0344.1>, 2019

983

984 Qin, J., Liang, S., Yang, K., Kaihotsu, I., Liu, R., and Koike, T.: Simultaneous estimation
985 of both soil moisture and model parameters using particle filtering method through the
986 assimilation of microwave signal. *Journal of Geophysical Research*, 114(D15), 1–13.

987 <https://doi.org/10.1029/2008JD011358>, 2009.

988

989 Rasmussen, J., Madsen, H., Jensen, K. H., and Refsgaard, J. C.: Data assimilation in
990 integrated hydrological modeling using ensemble Kalman filtering: evaluating the effect
991 of ensemble size and localization on filter performance. *Hydrology and Earth System
992 Sciences*, 19(7), 2999–3013. <https://doi.org/10.5194/hess-19-2999-2015>, 2015.



993

994 Ridler, M.-E., H. Madsen, S. Stisen,, S. Bircher, and R. Fensholt, Assimilation of SMOS-
995 derived soil moisture in a fully integrated hydrological and soil-vegetation-atmosphere
996 transfer model in Western Denmark, *Water Resour. Res.*, 50, 8962 - 8981,
997 <https://doi.org/10.1002/2014WR015392>, 2014.

998

999 Sakamoto, T., et al.: Detecting temporal changes in the extent of annual flooding within
1000 the Cambodia and the Vietnamese Mekong Delta from MODIS time-series imagery.
1001 *Remote Sensing of Environement*, 109, 295-313.
1002 <https://doi.org/10.1016/j.rse.2007.01.011>, 2007.

1003

1004 Sawada, Y. and Koike, T.: Simultaneous estimation of both hydrological and ecological
1005 parameters in an eco-hydrological model by assimilating microwave signal, *Journal of*
1006 *Geophysical Research – Atmospheres*, 119, 8839-8857,
1007 <https://doi.org/10.1002/2014JD021536>, 2014.

1008



1009 Sawada, Y., Koike, T., and Walker, J. P.: A land data assimilation system for simultaneous
1010 simulation of soil moisture and vegetation dynamics, *Journal of Geophysical Research –*
1011 *Atmospheres*, 120, 5910-5930, <https://doi.org/10.1002/2014JD022895>, 2015

1012

1013 Sawada, Y., Nakaegawa, T, and Miyoshi, T.: Hydrometeorology as an inversion problem:
1014 Can river discharge observations improve the atmosphere by ensemble data assimilation?,
1015 *Journal of Geophysical Research – Atmospheres*, 123, 848-860,
1016 <https://doi.org/10.1002/2017JD027531>, 2018

1017

1018 Sellers, P. J., et al.: A revised land surface parameterization (SiB2) for atmospheric GCMs.
1019 Part I: Model formulation. *Journal of Climate*. [https://doi.org/10.1175/1520-0442\(1996\)009<0676:ARLSPF>2.0.CO;2](https://doi.org/10.1175/1520-0442(1996)009<0676:ARLSPF>2.0.CO;2), 1996

1021

1022 Shrestha, P., Sulis, M., Masbou, M., Kollet, S., and Simmer, C.: A Scale-Consistent
1023 Terrestrial Systems Modeling Platform Based on COSMO, CLM, and ParFlow. *Monthly
1024 Weather Review*, 142(9), 3466–3483. <https://doi.org/10.1175/MWR-D-14-00029.1>, 2014

1025



1026 Snyder, C., Bengtsson, T., Bickel, P., and Anderson, J.: Obstacles to High-Dimensional
1027 Particle Filtering. *Monthly Weather Review*, 136(12), 4629–4640.
1028 <https://doi.org/10.1175/2008MWR2529.1>, 2008
1029
1030 Tian, W., Li, X., Cheng, G. D., Wang, X. S., and Hu, B. X.: Coupling a groundwater
1031 model with a land surface model to improve water and energy cycle simulation.
1032 *Hydrology and Earth System Sciences*, 16(12), 4707–4723. <https://doi.org/10.5194/hess-16-4707-2012>, 2012.
1033
1034
1035 Van Genuchten, M. T.: A closed-form equation for predicting the hydraulic conductivity
1036 of unsaturated soils, *Soil Science Society of America Journal*, 44, 892–898, 1980.
1037
1038 Van Leeuwen, P., J.: Particle Filtering in Geophysical Systems, *Monthly Weather Review*,
1039 137, 4089–4114, <https://doi.org/10.1175/2009MWR2835.1>, 2009
1040
1041 Verbeeck, H., Peylin, P., Bacour, C., Bonal, D., Steppe, K., and Ciais, P.: Fluxes in
1042 Amazon forests: Fusion of eddy covariance data and the ORCHIDEE model. *Journal of
1043 Geophysical Research*, 116(G2), 1–19. <https://doi.org/10.1029/2010JG001544>, 2011.



1044

1045 Vrugt, J. A., ter Braak, C. J. F., Clark, M. P., Hyman, J. M., and Robinson, B. A.:
1046 Treatment of input uncertainty in hydrologic modeling: Doing hydrology backward with
1047 Markov chain Monte Carlo simulation. *Water Resources Research*, 44, 1–15.
1048 <https://doi.org/10.1029/2007WR006720>, 2008.

1049

1050 Vrugt, J. A., ter Braak, C. J. F., Diks, C. G. H., and Schoups, G.: Hydrologic data
1051 assimilation using particle Markov chain Monte Carlo simulation: Theory, concepts and
1052 applications. *Advances in Water Resources*, 51, 457–478.
1053 <https://doi.org/10.1016/j.advwatres.2012.04.002>, 2013.

1054

1055 Williams, J. L., and Maxwell, R. M.: Propagating Subsurface Uncertainty to the
1056 Atmosphere Using Fully Coupled Stochastic Simulations. *Journal of Hydrometeorology*,
1057 12(4), 690–701. <https://doi.org/10.1175/2011JHM1363.1>, 2011.

1058

1059 Wood, E. F., et al.: Hyperresolution global land surface modeling : Meeting a grand
1060 challenge for monitoring Earth's terrestrial water, *Water Resources Research*, 47,
1061 <https://doi.org/10.1029/2010WR010090>, 2011.



1062

1063 Yan, H., and Moradkhani, H.: Combined assimilation of streamflow and satellite soil
1064 moisture with the particle filter and geostatistical modeling. *Advances in Water Resources*,
1065 94, 364–378. <https://doi.org/10.1016/j.advwatres.2016.06.002>, 2016.

1066

1067 Yang, K., Koike, T., Kaihatsu, I., and Qin, J.: Validation of a Dual-Pass Microwave Land
1068 Data Assimilation System for Estimating Surface Soil Moisture in Semiarid Regions.
1069 *Journal of Hydrometeorology*, 10(3), 780–793. <https://doi.org/10.1175/2008JHM1065.1>,
1070 2009.

1071

1072 Yang, K., Watanabe, T., Koike, T., Li, X., Fujii, H., Tamagawa, K., and Ishikawa, H.:
1073 Auto-calibration System Developed to Assimilate AMSR-E Data into a Land Surface
1074 Model for Estimating Soil Moisture and the Surface Energy Budget. *Journal of the
1075 Meteorological Society of Japan*, 85A, 229–242. <https://doi.org/10.2151/jmsj.85A.229>,

1076 2007.

1077

1078 Zhang, D., Madsen, H., Ridler, M. E., Refsgaard, J. C., and Jensen, K. H.: Impact of
1079 uncertainty description on assimilating hydraulic head in the MIKE SHE distributed



1080 hydrological model, *Advances in Water Resources*, 86, 400-413,

1081 <https://doi.org/10.1016/j.advwatres.2015.07.018>, 2015.

1082

1083 Zhang, F., Snyder, C., and Sun, J.: Impacts of Initial Estimate and Observation

1084 Availability on Convective-Scale Data Assimilation with an Ensemble Kalman Filter.

1085 *Monthly Weather Review*, 132, 1238–1253, <https://doi.org/10.1175/1520->

1086 [0493\(2004\)132<1238:IOIEAO>2.0.CO;2](https://doi.org/10.1175/1520-132-1238.IOIEAO2.0.CO;2), 2004

1087

1088 Zhang, H., Kurtz, W., Kollet, S., Vereecken, H., and Franssen, H. J. H.: Comparison of

1089 different assimilation methodologies of groundwater levels to improve predictions of root

1090 zone soil moisture with an integrated terrestrial system model. *Advances in Water*

1091 *Resources*, 111, 224–238. <https://doi.org/10.1016/j.advwatres.2017.11.003>, 2018.

1092

1093



1094

1095

096

097 **Table 1.** Configuration of the data assimilation experiments in section 3.1.

	hydraulic conductivity [m/h]	observation's location [m]
LOW_K-UP_O	0.005	2500
LOW_K-DOWN_O	0.005	1500
HIGH_K-UP_O	0.02	2500
HIGH_K-DOWN_O	0.02	1500

098

099 **Table 2.** Configuration of the data assimilation experiments in section 3.2

	overland flows	observing network
noOF_NoDA	none	no data assimilation
noOF_DA_obs1	none	Figure 7a
noOF_DA_obs9	none	Figure 7b
noOF_DA_obs361	none	Figure 7c
OF_NoDA	simulated	no data assimilation
OF_DA_obs1	simulated	Figure 7a
OF_DA_obs9	simulated	Figure 7b
OF_DA_obs361	simulated	Figure 7c

100

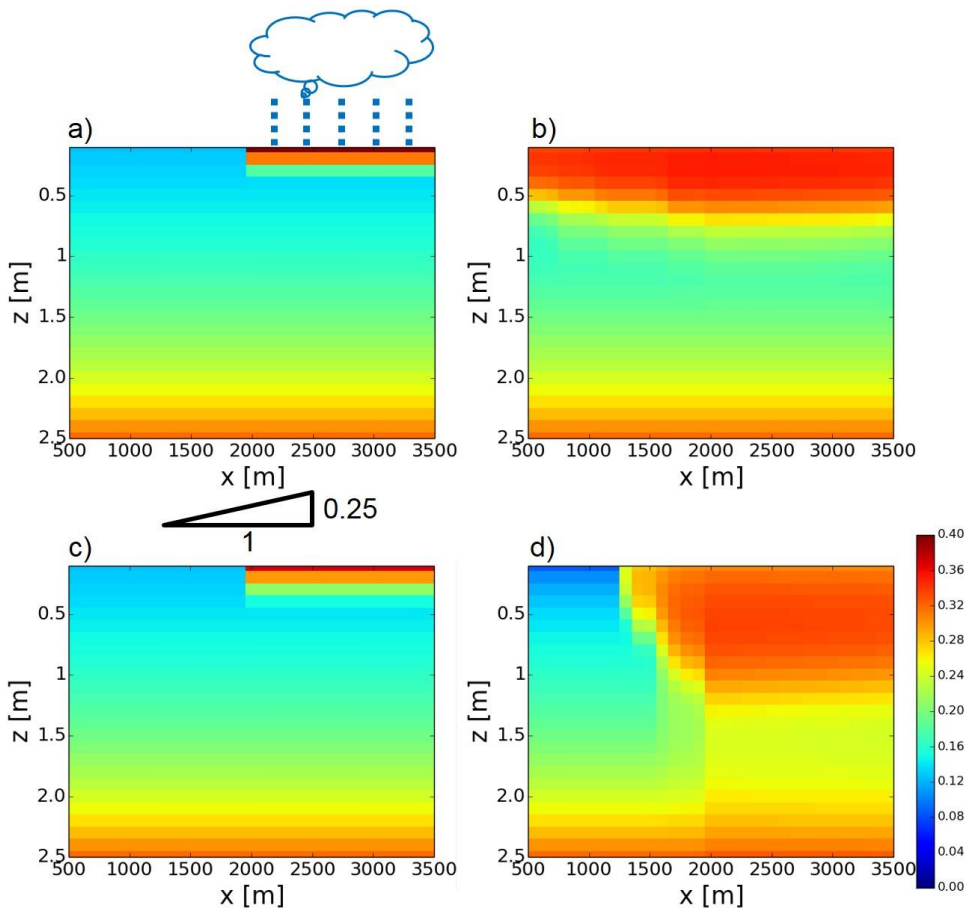
101

102

103



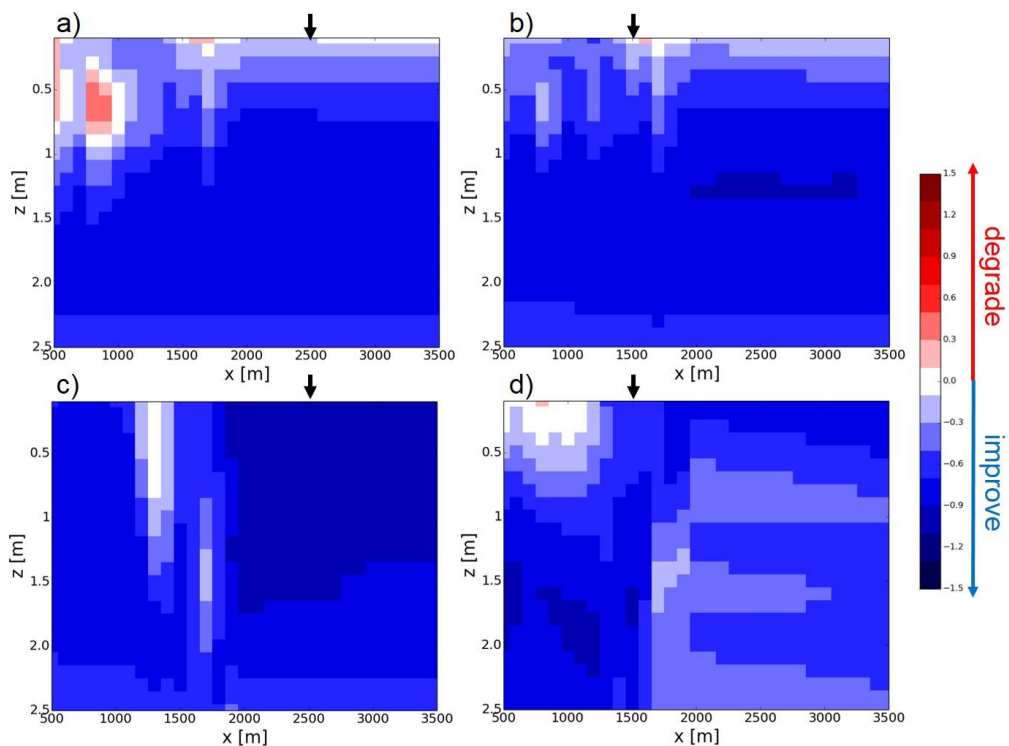
104



105

106 **Figure 1.** Distributions of volumetric soil moisture simulated by the synthetic reference runs. (a) The
107 distribution of volumetric soil moisture [m^3/m^3] simulated by the LOW_K synthetic reference run at $t = 0\text{h}$.
108 The schematic of the configuration of the synthetic reference runs is also shown (see also section 3). (b) same
109 as (a) but at $t = 130\text{h}$. (c,d) same as (a,b) but for the HIGH_K synthetic reference run.

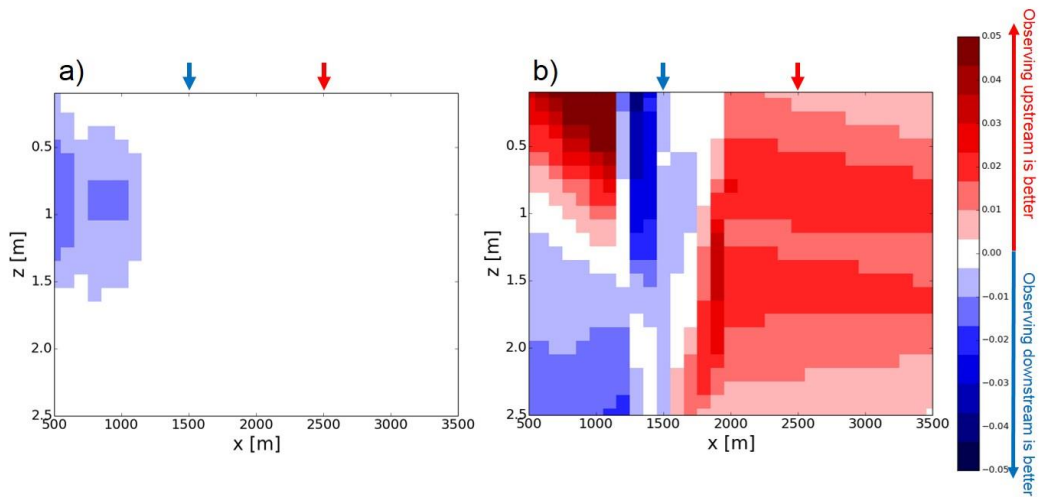
110



111

112 **Figure 2.** The improvement rates of the (a) LOW_K-UP_O, (b) LOW_K-DOWN_O, (c) HIGH_K_UP_O,
113 (d) HIGH_K-DOWN_O experiments (see Table 1 and section 3). Black arrows show the locations of the soil
114 moisture observations in each experiment.

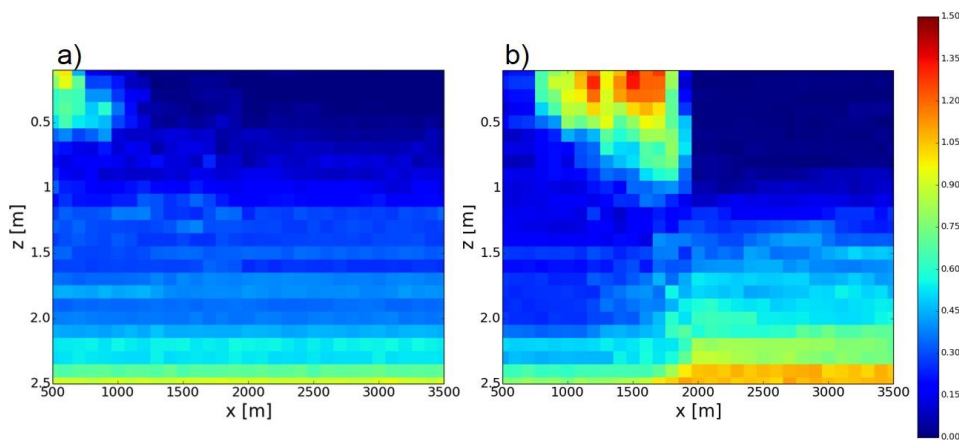
115



116

117 **Figure 3.** (a) The difference of time-mean RMSEs between the LOW_K-UP_O and LOW_K-DOWN_O
118 experiments (see Table 1 and section 3). Red (blue) color indicates that the observations in the upper (lower)
119 part of the slope reduce time-mean RMSE by data assimilation better than those in the lower (upper) part of
120 the slope (see also arrows which are the locations of the observations). (b) same as (a) but for the difference
121 between the HIGH_K-UP_O and HIGH_K-DOWN_O experiments.

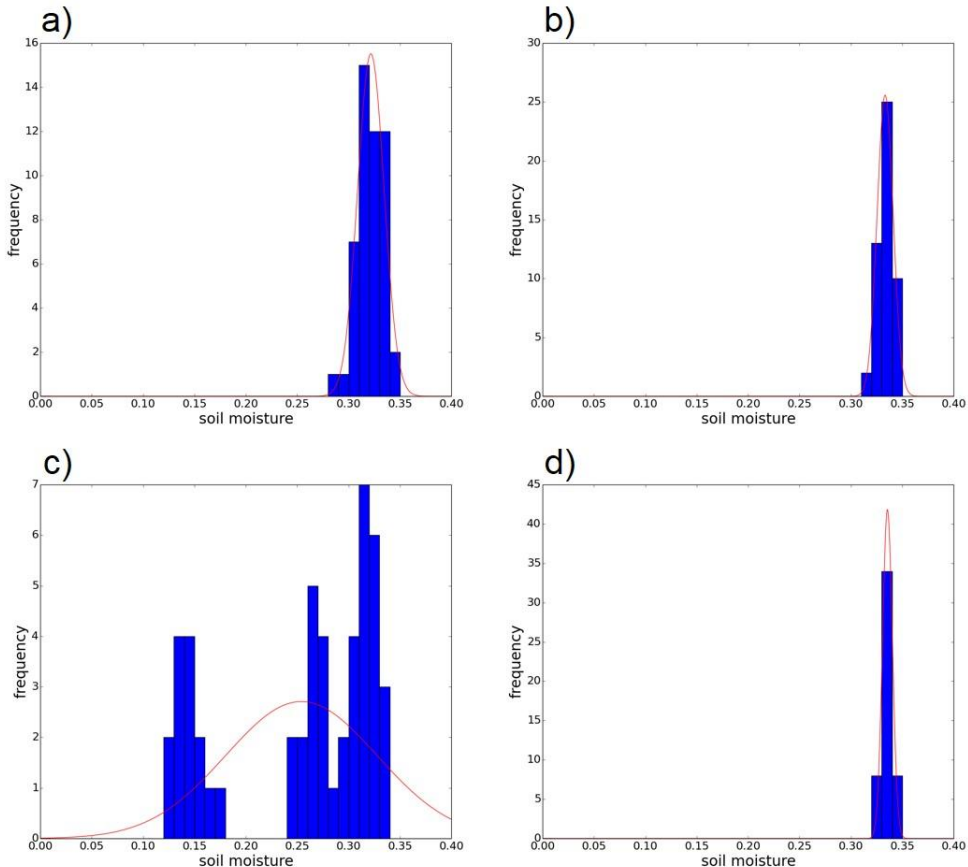
122



123

124 **Figure 4.** The Kullback-Leibler divergence of the NoDA experiment generated by (a) the LOW_K reference
125 and (b) the HIGH_K reference at $t = 130\text{h}$ (see also Figure 1b and 1d).

126



127

128 **Figure 5.** (a) The histogram (blue bars) of the volumetric soil moisture simulated by the NoDA experiment

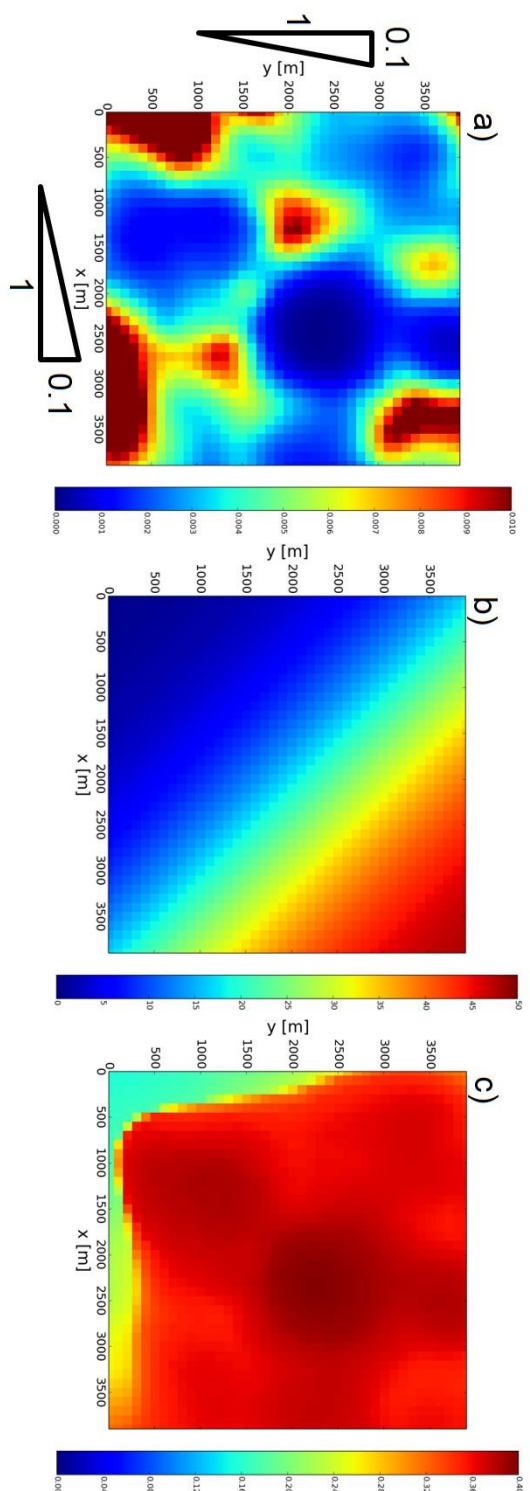
129 (see section 3) with the LOW_K reference at $x=1500\text{m}$, $z=0.5\text{m}$, and $t=130\text{h}$ (see also Figure 4). Red line

130 shows the Gaussian distribution with the mean and variance sampled by the ensemble. (b) same as (a) but at

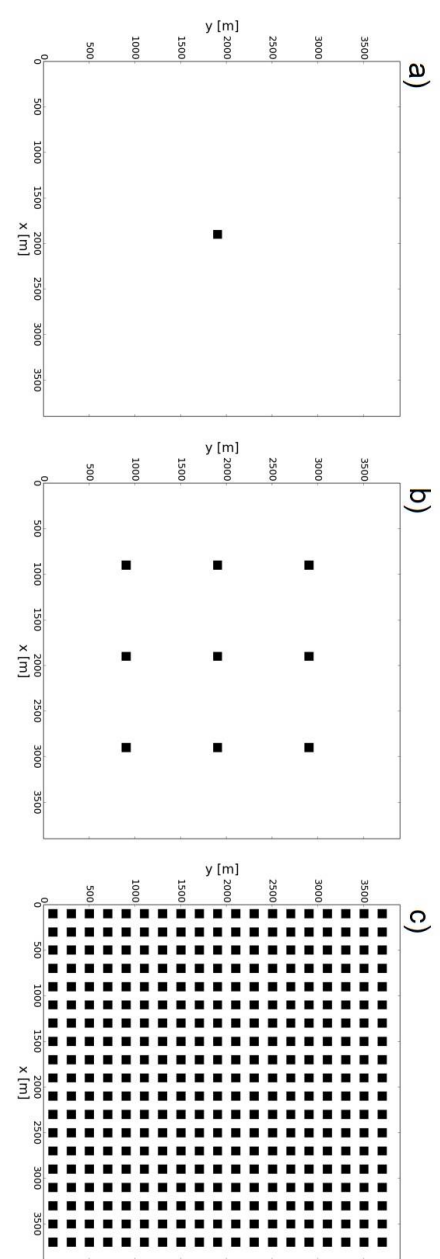
131 $x=2500\text{m}$, $z=0.5\text{m}$, and $t=130\text{h}$. (c) same as (a) but for the HIGH_K reference. (d) same as (c) but at $x=2500\text{m}$,

132 $z=0.5\text{m}$, and $t=130\text{h}$.

133



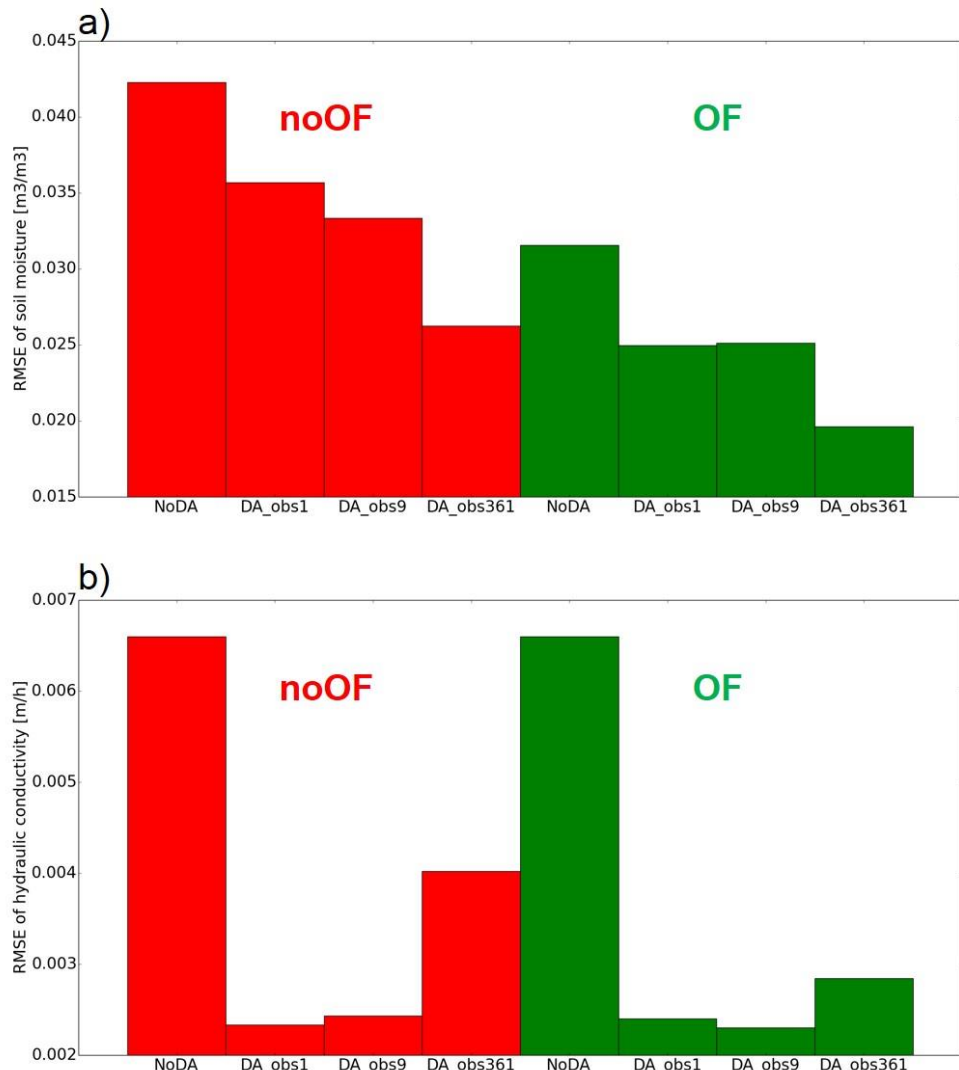
135
136 **Figure 6.** (a) Distribution of surface saturated hydraulic conductivity [m/h] in the synthetic reference. (b) Distribution of rainfall rate [mm/h] in the synthetic
137 reference. (c) Surface volumetric soil moisture [m^3/m^3] at $t = 5$ [h] in the synthetic reference.
138



139 **Figure 7.** Observing networks. Black boxes are observed grids. (a) obs1, (b) obs9, (c) obs361 See also section 3.2.1.
140
141

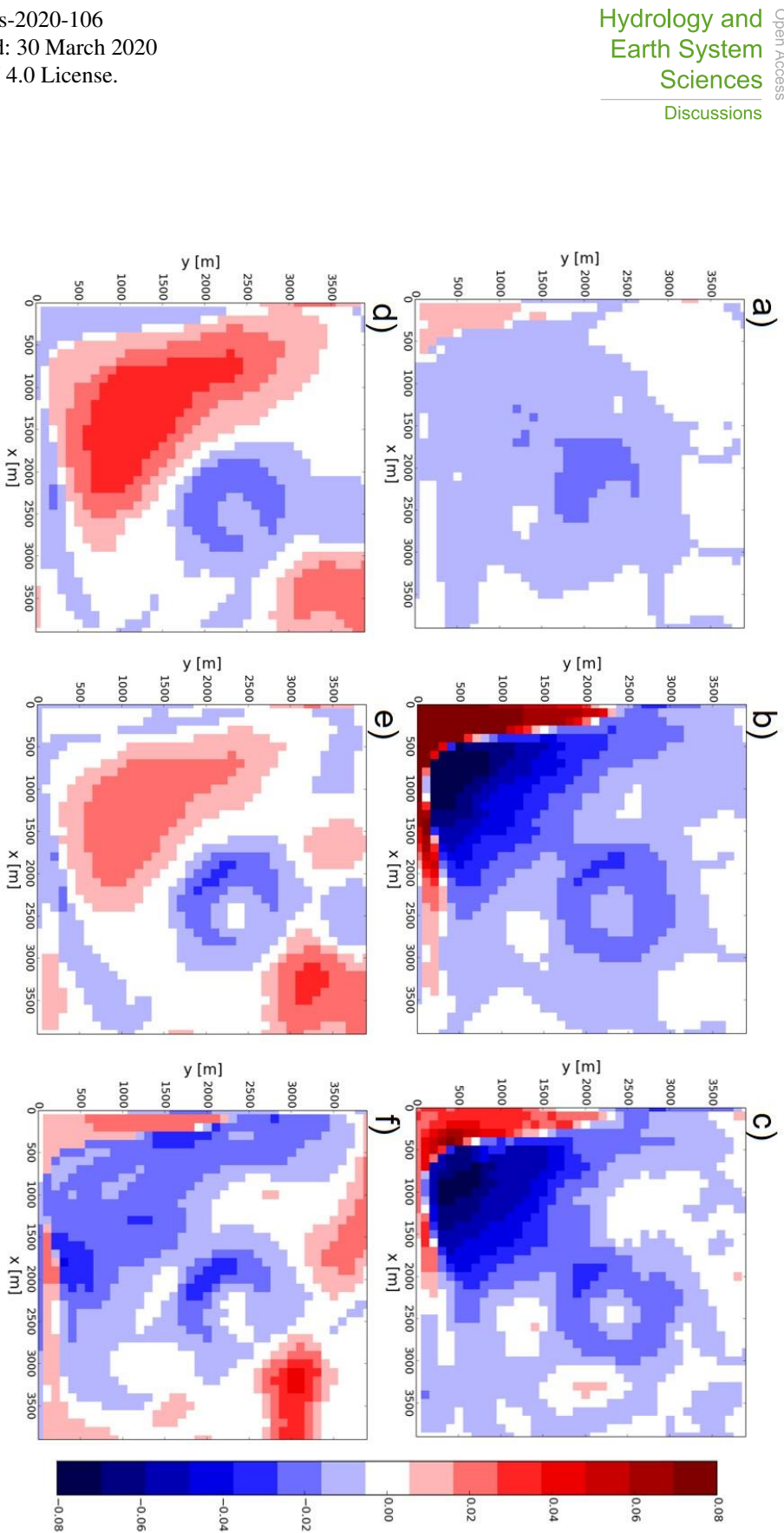


142



143

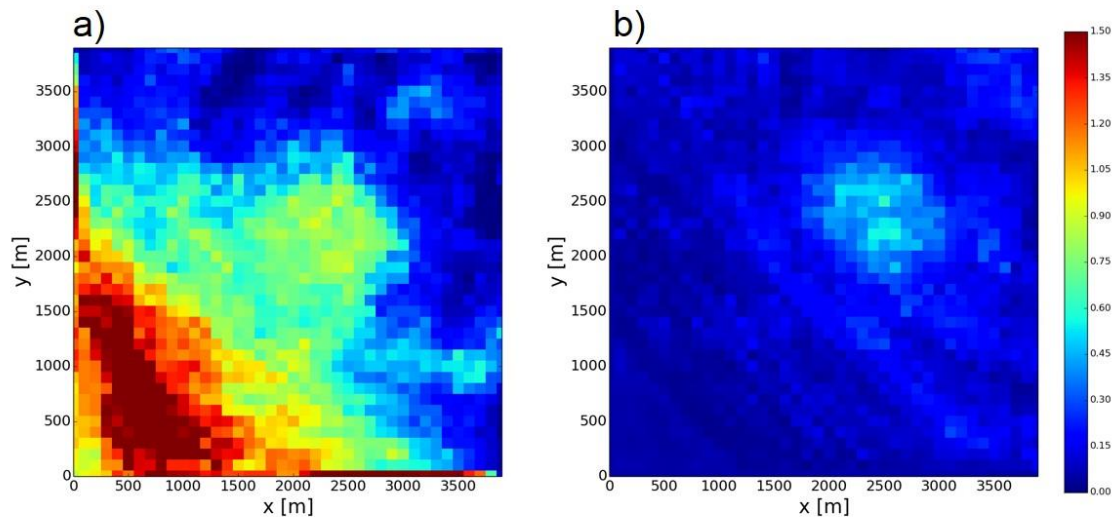
144 **Figure 8.** Time-mean RMSEs of the estimation of (a) soil moisture and (b) hydraulic conductivity. Red and
145 green bars are results of the noOF and OF configuration, respectively (see section 3.2.1 and Table 2).
146



147
148 **Figure 9.** Differences of time-mean soil moisture RMSEs between the DA experiments and the OF_NoDA experiment. (a) OF_DA_obs1, (b) OF_DA_obs9, (c)
149 OF_DA_obs361 (d) noOF_DA_obs1, (e) noOF_DA_obs9, (f) noOF_DA_obs361.



150



151

152 **Figure 10.** The Kullback-Leibler divergence of ensemble members generated by the (a) OF_NoDA and (b)
153 noOF_NoDA experiments at $t = 4$ [h].

154

155